



**NTNU – Trondheim**  
Norwegian University of  
Science and Technology

# Wind tunnel model testing of offshore platforms

**Ida Sinnes Abrahamsen**

Master of Science in Product Design and Manufacturing

Submission date: June 2012

Supervisor: Lars Sætran, EPT

Norwegian University of Science and Technology  
Department of Energy and Process Engineering



EPT-M-2012-10

**MASTER THESIS**

for

Ida Sinnes Abrahamsen

Spring 2012

Wind tunnel model testing of offshore platforms

Modelltesting av offshore plattformer i vindtunnel

The stability of offshore oil/gas floating platforms is of concern and platform design is regulated according to requirements by the Norwegian Maritime Directorate. As part of the stability analysis the response of the platform to severe environmental loads from wind and sea loads are tested and measured using model tests in a wind tunnel. The testing requirements and procedures are described in NMD Regulations “Appendix to §8 – Wind tunnel test procedure”.

Several platforms have been analysed wrt. wind/sea loads and platform stability using the wind tunnel in the Aerodynamics Lab at the department and experience has been established in the different modelling techniques involved in the model building and testing process, e.g. using roughness elements on cylindrical structures to ensure flow separation at realistic positions, using length scale ratios based on correct drag modelling, and modelling aspects of the incoming atmospheric wind and sea flow.

The candidate will utilize existing platform models and the wind tunnel with associated measuring equipment to perform a stability analysis according to the NMD regulations. Based on the results obtained and the experience gained –a critical evaluation of the accuracy of the modelling techniques and the experimental details involved in the testing should be done. The elements in the experiments that contribute most to the inaccuracy of the test should be identified, with proposals for how to improve the accuracy.

-- ” --

Within 14 days of receiving the written text on the master thesis, the candidate shall submit a research plan for his project to the department.

When the thesis is evaluated, emphasis is put on processing of the results, and that they are presented in tabular and/or graphic form in a clear manner, and that they are analyzed carefully.

The thesis should be formulated as a research report with summary both in English and Norwegian, conclusion, literature references, table of contents etc. During the preparation of the text, the candidate should make an effort to produce a well-structured and easily readable report. In order to ease the evaluation of the thesis, it is important that the cross-references are correct. In the making of the report, strong emphasis should be placed on both a thorough discussion of the results and an orderly presentation.

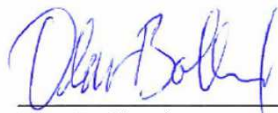
The candidate is requested to initiate and keep close contact with his/her academic supervisor(s) throughout the working period. The candidate must follow the rules and regulations of NTNU as well as passive directions given by the Department of Energy and Process Engineering.

Risk assessment of the candidate's work shall be carried out according to the department's procedures. The risk assessment must be documented and included as part of the final report. Events related to the candidate's work adversely affecting the health, safety or security, must be documented and included as part of the final report.

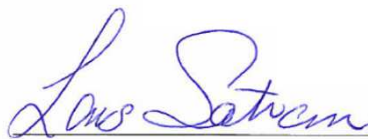
Pursuant to "Regulations concerning the supplementary provisions to the technology study program/Master of Science" at NTNU §20, the Department reserves the permission to utilize all the results and data for teaching and research purposes as well as in future publications.

The final report is to be submitted digitally in DAIM. An executive summary of the thesis including title, student's name, supervisor's name, year, department name, and NTNU's logo and name, shall be submitted to the department as a separate pdf file. Based on an agreement with the supervisor, the final report and other material and documents may be given to the supervisor in digital format.

Department of Energy and Process Engineering, 16. January 2012



Olav Bolland  
Department Head



Lars Sætran  
Academic Supervisor

Research Advisors: Lars Morten Bardal

## Acknowledgements

This master thesis has been carried out at the Department of Energy and Process Engineering at The Norwegian University of Science and Technology in the spring 2012. Hopefully this report will familiarize the reader with the basics behind wind tunnel platform testing.

I would like to thank my supervisor, Professor Lars R. Sætran for his support, help and guidance throughout this project. I also want to thank the workshop supervisor at the "Aerodynamics Lab", Arnt Egil Kolstad, for construction of test models and helping me with all technical preparations for the experiments. A special thanks to Lars Morten Bardal for sharing his knowledge about wind tunnel experimenting and for always having time to answer my questions.

Trondheim, June 2012

A handwritten signature in cursive script that reads "Ida Sinnes Abrahamsen".

Ida Sinnes Abrahamsen

## Summary

The purpose of this thesis is to highlight some of the areas of interest when it comes to wind tunnel experimenting of offshore platforms regarding stability concerns such as critical angles and wind overturning moment. Some important factors include design of tower geometry, the effect of surface roughness on drag, methods of calculating blockage corrections of wall interference and the generation of an atmospheric boundary layer to resemble full-scale conditions.

Data obtained from wind tunnel experiments with two different models have been compared and discussed according to the areas of interest as mentioned above. Testing of platforms was done at NTNU with a six-component balance, measuring forces of drag, side and lift and moment of pitch, roll and yaw with increments of  $10^\circ$  the whole  $360^\circ$  to account for wind coming from all directions.

Two geometries were tested for the tower members, one with a circular cross-section which was smaller than scale and another with a square cross-section in correct scale. There was noticeable change in both global forces and moments.

Blockage corrections caused by wall interference were researched from different sources and reviewed, and it was apparent that it is still an area with lots of uncertainty. Consensus was that an area ratio of maximum 0.10 should be abided in any case and that the simplified method of Pope is widely used.

An atmospheric boundary layer was simulated at NTNU using trial-and-error and the validity of this was confirmed by comparing experimental data with theoretical data regarding the velocity profile, turbulence intensity and energy spectrum.

For the experiments of surface roughness on an individual circular cylinder and the corresponding change in drag, a simple three-component balance was used. The cylinder represents the platform legs. Two types of surface roughness were tested, first a plain wooden surface and then with a layer of coarse sand applied to the whole surface. It was seen that the rougher surface provoked an earlier transition to a turbulent boundary layer, causing an earlier drop in drag which is a better fit to estimated full-scale characteristics.

Finally, the element that contributes most to the inaccuracy of the experiments is shown to be the difficulty of geometric similarity. Further investigation is needed.

## Sammendrag

Formålet med denne oppgaven er å undersøke visse områder rundt testing av oljeplattformer i vindtunnel. Viktige parametre er geometrien og skalering av modellen, påvirkningen av overflateruhet for målinger av luftmotstand, hvordan korrigere for påvirkningen av veggene på strømmingen i vindtunnelen og hvordan simulere et korrekt atmosfærisk grensesjikt i tunnelen som gjengir virkeligheten.

Data fra testene med ulike modeller har blitt sammenlignet og diskutert med hensyn til de viktige parametrene nevnt ovenfor. Testing av plattformene er gjort på NTNU med en seks-komponents vekt som måler luftmotstand, sidekraft og løft med tilsvarende rotasjonsmomenter for hver 10ende grad de hele 360 gradene for å simulere vind fra alle retninger.

To ulike geometrier ble testet for plattformtårnene, en med et sirkulært tverrsnitt som var mindre enn skala og en med firkantet tverrsnitt som var i skala. Resultatene viste en merkbar forskjell for de målte krefter og momenter for de to tilfellene.

Blokkering av luftstrømninger på grunn av påvirkninger fra vindtunnelveggen har blitt undersøkt i forhold til ulike metoder, og det var tydelig et fagfelt i utvikling. Det var enighet om at arealforholdet mellom modellens og vindtunnelens tverrsnitt ikke burde overstige 0.10 og at metoden til Pope er ofte brukt for sin enkelhet.

Et atmosfærisk grensesjikt har blitt simulert av NTNU ved prøving og feiling og validering av sjiktet har blitt vurdert i forhold til anbefalinger fra litteraturen og NMD i forhold til hastighetsprofil, turbulensintensitet og energispektrum.

For eksperimentene med overflateruhet på en individuell sirkulær sylinder og den følgende endringen i luftmotstand, en enkel tre-komponents balansevekt ble brukt. Sylindere skal representere plattformbeina. To ulike overflater ble testet, først ubehandlet tre og deretter med et lag av grove sandkorn på hele overflaten. Det viste seg at en ruere overflate fremskyndet overgangen til et mer turbulent grensesjikt, som igjen førte til en tidligere nedgang i luftmotstand. Dette var mer i samsvar med forventet luftmotstand for fullskala forhold.

Til slutt, den faktoren som bidrar mest til unøyaktighet i eksperimentene viser seg å være utilstrekkelig geometrisk likhet for skalert modell. Videre undersøkelser behøves.

# Contents

<b>1</b>	<b>Introduction</b>	<b>1</b>
<b>2</b>	<b>Theory</b>	<b>3</b>
2.1	Wind tunnel test procedure . . . . .	3
2.1.1	Regulations . . . . .	4
2.1.2	Model and scale effects . . . . .	4
2.1.3	Wind profile . . . . .	4
2.1.4	Measurements . . . . .	4
2.2	Non-dimensional coefficients . . . . .	5
2.2.1	Buckingham PI theorem . . . . .	5
2.2.2	Reynolds number . . . . .	7
2.3	Forces and moments on an immersed body . . . . .	7
2.3.1	Force and moment coefficients . . . . .	8
2.3.2	Drag . . . . .	9
2.3.3	Streamlined or bluff objects . . . . .	9
2.3.4	Bodies with sharp edges . . . . .	10
2.3.5	Transition from laminar to turbulent boundary layer and flow separation . . . . .	10
2.4	Reynolds number vs drag coefficient . . . . .	11
2.4.1	Critical region . . . . .	12
2.4.2	Surface roughness . . . . .	13
2.5	Atmospheric boundary layer . . . . .	13
2.5.1	Boundary layer profile . . . . .	15
2.5.2	Theoretical design versus experimental design . . . . .	16
2.5.3	Turbulence intensity . . . . .	19
2.5.4	Wind spectrum . . . . .	21
2.5.5	Limitations . . . . .	22
2.6	Wind tunnel blockage . . . . .	23
2.6.1	Pope and Harper . . . . .	27
2.6.2	Maskell . . . . .	27
2.6.3	Hackett . . . . .	28
2.6.4	Comparison between methodologies . . . . .	28
2.7	Wind tunnel velocity . . . . .	29
2.7.1	Venturi effect . . . . .	29



2.7.2	Pitot tube . . . . .	33
<b>3</b>	<b>Experimental equipment</b>	<b>34</b>
3.1	Wind tunnels . . . . .	34
3.2	Calibration and linearity . . . . .	35
3.3	Six-component balance . . . . .	35
3.3.1	Calibration . . . . .	37
3.4	Three-component balance . . . . .	37
3.4.1	Calibration . . . . .	38
3.5	Venturi principle . . . . .	39
3.6	Pitot tube . . . . .	39
3.7	Setra pressure transducer . . . . .	39
3.7.1	Calibration . . . . .	39
3.8	Manometer . . . . .	40
3.9	National Instruments cDAQ-9172 . . . . .	41
3.10	NI LabVIEW . . . . .	41
<b>4</b>	<b>Experiments and results</b>	<b>42</b>
4.1	Tower framework . . . . .	43
4.2	Atmospheric boundary layer . . . . .	52
4.3	Flow around a circular cylinder . . . . .	55
4.3.1	Experiment set-up . . . . .	55
4.3.2	Comparison between built-in pressure differential and pitot tube measurements . . . . .	56
4.3.3	Cylinder surface roughness . . . . .	56
4.3.4	Experimental results and discussion . . . . .	59
4.4	Experimental uncertainty . . . . .	59
<b>5</b>	<b>Conclusion</b>	<b>62</b>
5.1	Platform legs and cylinder drag . . . . .	62
5.2	Tower framework . . . . .	63
5.3	Atmospheric boundary layer . . . . .	63
5.4	Wind tunnel blockage . . . . .	64
5.5	Uncertainty . . . . .	64
5.6	Concluding remarks . . . . .	64
<b>A</b>	<b>NMD Regulations</b>	<b>69</b>
<b>B</b>	<b>Maskell's correction factors</b>	<b>72</b>

# List of Figures

2.1	Forces and moments on an immersed body with corresponding axis	8
2.2	Boundary layer separation	10
2.3	Typical $C_D - Re$ graph for a circular cylinder	11
2.4	Critical region	12
2.5	Surface roughness[16]	13
2.6	Illustrative velocity profiles for different types of terrain	14
2.7	Velocity profile within boundary layer	15
2.8	Boundary layer velocity profile based on the power law with different values of $\alpha$ [13]	16
2.9	Atmospheric boundary layer set-up in the wind tunnel	17
2.10	Theoretical versus experimental wind velocity profile	19
2.11	Turbulence intensity experimental results	21
2.12	Wind spectrum at $z = 30$ m	22
2.13	Ekman spiral of wind	23
2.14	Increase in velocity due to solid and wake blockage[10]	24
2.15	Zero angle and rotation illustration of model	25
2.16	Blockage ratio	26
2.17	Data comparison of different correction methods	30
2.18	Comparison between methods for a range of values of $C_D$	31
2.19	Wind tunnel cross-sections	32
2.20	Pitot tube	33
3.1	Linearity	35
3.2	Overview of the set-up of the six component balance	36
3.3	Three-component balance weight beams	37
3.4	Three component balance	38
3.5	Calibration of transducer	40
3.6	Manometer characteristics	40
4.1	System of axes	42
4.2	Model of platform A	43
4.3	Model A, tower 1	44
4.4	Model A, tower 2	44
4.5	Model A, tower 1: forces and moments coefficients	46
4.6	Model A, tower 2: forces and moments coefficients	47

4.7	Model A, tower 1 and 2 forces comparison . . . . .	48
4.8	Model A, tower 1 and 2 moments comparison . . . . .	49
4.9	Model B, forces comparison between circular and square (subnote w) members . . . . .	50
4.10	Model B, moments comparison between circular and square (subnote w) members . . . . .	51
4.11	Comparison of forces with and without (noted _1) a simulated atmospheric boundary layer . . . . .	53
4.12	Comparison of moments with and without (noted _1) a simulated atmospheric boundary layer . . . . .	54
4.13	Cylinder measurements and cross-section . . . . .	55
4.14	Dummy cylinders and boundary layer . . . . .	55
4.15	Experimental set-up with cylinder . . . . .	56
4.16	Test cylinder surfaces . . . . .	57
4.17	Cylinder $C_D - Re$ data . . . . .	58
B.1	Blockage correction factors, $\epsilon$ and $m$ given a certain aspect ratio $\frac{S}{A}$ (left) Two-dimensional flow (right) Three-dimensional flow [1]	72

# List of Tables

2.1	Variables of an immersed body . . . . .	5
2.2	Spire and barrier dimensions at NTNU . . . . .	17
3.1	Instrumentation overview . . . . .	35
3.2	Calibration factors R1-R7 . . . . .	37
4.1	Details of the different towers . . . . .	44
4.2	Components of measurements . . . . .	61

# Chapter 1

## Introduction

The stability of offshore oil/gas floating platforms is of lasting concern and platform design is regulated according to requirements by the Norwegian Maritime Directorate (NMD). As part of the stability analysis, the response of the platform to environmental loads such as wind and sea loads are tested and measured using model tests in a wind tunnel.

In recent years, the importance of floating platforms and other offshore structures have increased, and many studies have been conducted to identify the validity of the current wind tunnel test procedures of platform stability.

One of the more important design considerations are wind-induced overturning moment. We want to know at what rotational angles the platform is more likely to turn over. The goal is to be able to test model platforms in such a way that it is comparable to full scale conditions, which includes geometric similarity and wind conditions. Some important influences include platform freeboard, roughness elements, heel angle, wind angle, deck layout, wind tunnel boundary layer, wall interference and tower framework.

The objective of this thesis is to highlight some of these influences by doing experiments on two existing platform models and compare researched theory with the practical results.

Roughness elements have been applied to cylindrical structures to ensure flow separation at realistic positions, and spires and barriers have been positioned at the wind tunnel entrance to simulate an atmospheric boundary layer at the test section. The increased velocity at the model caused by wall interference increases with larger models and must be accounted for in the calculation of coefficients.

The first part of this thesis will consist of a literature study of required theoretical background information on the subject of wind tunnel testing. That includes NMD regulations, the use of non-dimensional coefficients, the importance of Reynolds number considerations, flow characteristics, forces and moments acting on a body with special attention given to drag and the changing characteristics based on surface and shape of the body, atmospheric boundary layer concerning velocity profile, turbulence intensity and energy spectrum, and wall interference blockage corrections.

The last part consist of the experiments done based on the information gathered in the literature study, and will be reviewed in accordance with the knowledge aquired.

# Chapter 2

## Theory

This section explains the theory behind wind tunnel testing. Floating structures, one of them oil/gas platforms, are being more commonly used in the exploration and production of offshore oil and gas reserves today. Thus, it is important to make an accurate assessment of environmental loading on the structure e.g. wind.

That means that we have to have an understanding of the mathematical relations and theories behind it, as well as a well-functioning wind tunnel and test procedure that follows the regulations.

### 2.1 Wind tunnel test procedure

In the case of floating oil platforms, wind is a major load to consider, and this is commonly tested in a wind tunnel with a model using a balance with the desired number of components, usually six, measuring; drag force, side force, lift force, pitching moment, rolling moment and yaw moment.

Since the platform is not fixed on the sea bed and has a high above-water/below-water ratio, the wind will make it turn, which means that the model should be tested from every angle seeing that the wind will come across the platform from every angle at full scale. At the critical wind angle, where the overturning moment is the largest, additional measurements should be done for several heeling angles.

There are some simplifications that has to be done regarding platform testing in the wind tunnel, seeing that there is a trade-off between accuracy and time and resources. One of them being neglecting the effects of dynamic wind effects, thus keeping the velocity steady and the subsequent load equally steady. In reality, this is inaccurate, as wind loading is dynamic and reacts to changes in the free surface of the sea. As this is difficult to account for, testing conditions are usually static.

### 2.1.1 Regulations

There are regulations one has to follow to perform qualified experiments with models in the wind tunnel, issued by the Norwegian Maritime Directorate (NMD). See appendix A for more information. Some of these items are presented in the following sections.

### 2.1.2 Model and scale effects

All structural details and equipment should be fitted to the model to make sure the measurements are as accurate as possible. That means that everything should be in the correct scale, unless geometric changes must be made to maintain non-dimensional coefficients like the Reynolds number and ensure same character of the flow for both model and full-scale conditions. This will be addressed later under section 4.1. In all cases, both the mean velocity profile and the turbulence characteristics over the structure is a top priority and should match what is expected in full scale. Modeling guidelines can be found in standards provided by NMD, ESDU etc. Such data is helpful to ensure that the wind characteristics in the wind tunnel is similar to wind characteristics in full scale.

### 2.1.3 Wind profile

According to the NMD regulations, the mean velocity profile, at the above water part, should be according to the power law:

$$\frac{V_H}{V_{10}} = \left[ \frac{H}{10} \right]^\alpha \quad (2.1)$$

where  $V_H$  is the mean velocity at height  $H$  above water level,  $V_{10}$  is the velocity at reference height and  $\alpha$  is an exponent chosen to represent ocean wind which should be between 0.11 - 0.14. More information about the profile choice in section 2.5.1.

The underwater part should be tested with an uniform flow. As part of the experiments, data sets from testing with and without an atmospheric boundary layer for the above water part will be compared and discussed in chapter 4.

The velocity profile according to the power law and the corresponding measured velocity profile should be presented in the report, as well as the turbulence intensity in the wind direction.

### 2.1.4 Measurements

Prior to each run, instrument calibration must be done. Three forces (side, drag and lift) and three moments (pitch, roll and yaw) should be measured and presented as non-dimensional coefficients, and the direction of the wind should be changed in steps of  $10^\circ$  the whole  $360^\circ$ . Illustration of the starting position of the model should be provided.



## 2.2 Non-dimensional coefficients

When we are talking about wind tunnel test procedures, one of the most important topics is dimensional analysis. Usually, we are looking at a downscaled model when testing in the wind tunnel. In that case, we need to make sure that the conditions for the wind tunnel model matches that of the full scale model.

The relationship between the different parameters should coincide, and certain dimensionless numbers should give the same result, e.g. Reynolds number and the force and moment coefficients. It should be noted that for a model scale between 1:100 to 1:200, it is virtually impossible to maintain the Reynolds similitude of a full scale test when the velocity is the same in full-scale as when testing and the working fluid is air at atmospheric pressure.

However, since the model consists of bluff body shapes, which are independent of the Reynolds number, the distortion may not be important, see section 2.3.4.

One of the methods to derive the relation between the parameters of dimensionless coefficients is the Buckingham PI theorem.

### 2.2.1 Buckingham PI theorem

Buckingham's theorem[16] only provides a way of generating sets of dimensionless parameters,  $\Pi$ s, and will not choose the most 'physically meaningful', which means that we have to have an understanding of basic physical equations and relations to make use of it.

If we look at a variable we want to measure, for example the force developed on the model, we make an intuitive guess to which parameters will be important. To make it simple, we only consider fluid density, fluid velocity, geometric dimension of the model and dynamic viscosity as variables (see equation 2.2).

$$F = f(\rho, V, L, \mu) = \rho^\alpha V^\beta L^\gamma \mu^\epsilon \quad (2.2)$$

Variables	F	$\rho$	V	L	$\mu$
Dimensions (SI units)	$\frac{kgm}{s^2}$	$\frac{kg}{m^3}$	$\frac{m}{s}$	$m$	$\frac{kg}{ms}$

Table 2.1: Variables of an immersed body

From table 2.1, we can find out the number of variables  $n$  and the maximum number of variables that cannot form a pi group  $j$ . In this case:  $n = n(F, \rho, V, L, \mu) = 5$ . The next step is to choose the maximum number of variables that cannot form a pi group because some of them have dimensions which is not present in the other variables. We choose three;  $\rho \left[ \frac{kg}{m^3} \right]$ ,  $V \left[ \frac{m}{s} \right]$  and  $L [m]$ . These are going to be our repeating variables and will be included in all pi groups, which is why we need to choose carefully. We can calculate the number

of relations between  $k$  dimensionless variables,  $k = n - j = 2$ . That means that we will have two  $\Pi$ s, where one pi group is a function of the other, seeing that they are all dimensionless. Firstly,  $\Pi_1$  contains the three repeating variables plus force. It is possible to choose a random exponent for the last variable, so let us choose 1.

$$\Pi_1 = \rho^\alpha V^\beta L^\gamma F = \left(\frac{kg}{m^3}\right)^\alpha \left(\frac{m}{s}\right)^\beta (m)^\gamma \left(\frac{kgm}{s^2}\right) = kg^0 m^0 s^0 \quad (2.3)$$

$$kg : \alpha + 1 = 0 \quad (2.4)$$

$$m : -3\alpha + \beta + \gamma + 1 = 0 \quad (2.5)$$

$$s : -\beta - 2 = 0 \quad (2.6)$$

$$\Rightarrow \alpha = -1 \quad (2.7)$$

$$\Rightarrow \beta = -2 \quad (2.8)$$

$$\Rightarrow \gamma = -2 \quad (2.9)$$

$$\Pi_1 = \rho^{-1} V^{-2} L^{-2} F = \frac{F}{\rho V^2 L^2} \quad (2.10)$$

Secondly, the last remaining variable  $\mu$  is used in  $\Pi_2$  instead of  $F$ . From experience, we choose the exponent of  $\mu$  to be -1.

$$\Pi_2 = \rho^\alpha V^\beta D^\gamma \mu^{-1} = \left(\frac{kg}{m^3}\right)^\alpha \left(\frac{m}{s}\right)^\beta (m)^\gamma \left(\frac{kg}{ms}\right)^{-1} = kg^0 m^0 s^0 \quad (2.11)$$

$$kg : \alpha - 1 = 0 \quad (2.12)$$

$$m : -3\alpha + \beta + \gamma + 1 = 0 \quad (2.13)$$

$$s : -\beta + 1 = 0 \quad (2.14)$$

$$\Rightarrow \alpha = 1 \quad (2.15)$$

$$\Rightarrow \beta = 1 \quad (2.16)$$

$$\Rightarrow \gamma = 1 \quad (2.17)$$

$$\Pi_2 = \rho^1 V^1 D^1 \mu^{-1} = \frac{\rho V D}{\mu} \quad (2.18)$$

The theorem guarantees that the functional relationship must be:

$$\frac{F}{\rho V^2 L^2} = f\left(\frac{\rho V D}{\mu}\right) \quad (2.19)$$

If we compare the known relation of the force coefficient from equation 2.21 and the result from equation 2.10, and recognize that the result from equation

2.18 contains a known quantity, the Reynolds number, we can reduce it to equation 2.20 which tells us that the force coefficient is a function of the Reynolds number.

$$C_F = f(Re) \quad (2.20)$$

$$C_F = \frac{F}{\frac{1}{2}\rho V^2 A} \quad (2.21)$$

### 2.2.2 Reynolds number

The Reynolds number is an important parameter for the wind tunnel experiments. It is a non-dimensional number that is defined by the ratio of inertial force,  $\frac{\rho V^2}{L}$ , and viscous force,  $\frac{\mu V}{L^2}$ . The characteristic length L is in some cases defined as a diameter D, e.g. when we are looking at circular objects in the experiment (see section 4.3.4).

$$Re = \frac{\rho V L}{\mu} = \frac{\rho V D}{\mu} = \frac{V D}{\nu} \quad (2.22)$$

In the case of wind tunnel experiments, since the velocity is the same for full-scale and wind tunnel testing, the Reynolds number will be in the order of the model scale (1:N, see equation 2.23). The question is, will this have an impact on the simulation of the atmospheric boundary layer or other variables when testing. Because the model mainly consists of sharp-edged objects (excluding platform legs) independent of the Reynolds number, it might not be an issue.

$$\frac{Re_{model}}{Re_{full-scale}} = \frac{1}{N} \quad (2.23)$$

## 2.3 Forces and moments on an immersed body

Any body when immersed in a flowing fluid will experience forces and moments from the flow. An arbitrary shaped and oriented body will experience forces and moments about all three coordinate axes, as seen in figure 2.1. It is common to choose one of the axis to be parallel to the flow and positive downstream.

In this case it is the drag force with the rolling moment about its axis. Drag is considered a flow loss and is the main obstacle for the body if it is to move against the flow.

Another important force is the force perpendicular to the drag force, and it is lift. This is usually useful in situations where we need to bear the weight of the body or fly, as the case is with airfoils. In our case, with the forces of wind acting upon a floating oil platform, lift is a major contributor to the overturning moment. The moment about the lift axis is called yaw. The third component is the side force, normal to the flow direction and does not give a gain or a loss.

It has a corresponding pitching moment about its axis.

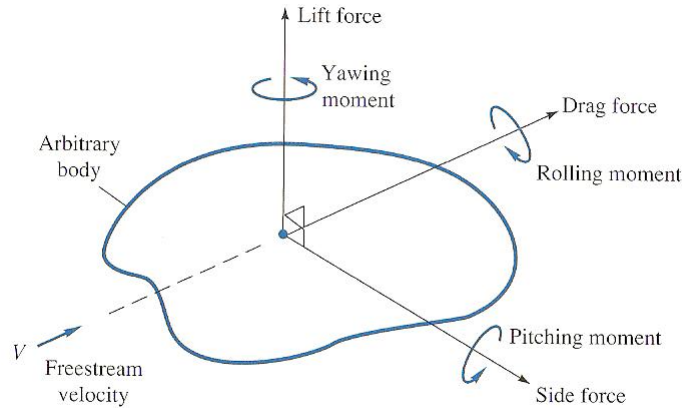


Figure 2.1: Forces and moments on an immersed body with corresponding axis

When the body has a symmetry axis about the lift-drag axis, with the fluid moving parallel to this axis, the side force, yaw and roll vanish. This reduces our problem to a two-dimensional case with two forces, lift and drag, and one moment, pitch. When testing the whole model in the large wind tunnel, we have to consider all three forces and moments.

Another simplification occurs when there is a second symmetry plane about the side-drag axis, and the fluid motion is parallel to the intersection between the two symmetry planes (called principal chord line of the body). This also eliminates lift and all moments, and leaves only drag. This includes wings without camber and cylinders, which is useful information when testing individual parts of the platform, as is the case with the platform legs in chapter 4.

### 2.3.1 Force and moment coefficients

When doing experiments of measuring forces and moments, we usually present the results as non-dimensional numbers. Let us take the drag force as an example. The drag coefficient then expresses the ratio of the drag force to the force produced by the dynamic pressure times the area:

$$C_D = \frac{F_D}{\frac{1}{2}\rho V^2 A} \quad (2.24)$$

The drag coefficient is defined by using a characteristic area  $A$ , which depends on the body shape. The characteristic area is usually either frontal area (body area as seen in the stream) or planform area (body area as seen from above). Frontal area is usually used for bodies such as spheres, cylinders and cars and subsequently platforms.

When evaluating data from experiments, it is important to note what kind of characteristic length (Reynolds number) and area (force and moment coefficients) that have been used to scale the results, especially if the results are to be used for comparison later.

### 2.3.2 Drag

When a body is moving through a fluid it is subject to a drag force that opposes the direction of the flow, and it can be divided into two components: frictional drag and pressure drag (similar for the corresponding coefficients, equation 2.25).

$$C_D = C_{Dp} + C_{Df} \quad (2.25)$$

Frictional drag is created between the fluid and the surface of the body it flows over. This friction is associated with shear stress and development of boundary layers and transitioning between laminar and turbulent flows. It is dependent upon the surface of the object in contact with the fluid and is important when looking at attached flows. It is also called viscous drag.

Pressure drag is created from the movements of the fluid across the object which generates circulation/eddy motions, and is the difference between the high pressure in the front stagnation region and the low pressure in the rear separated region. This drag depends on the cross-sectional area of the object and is important when looking at separated flows. It is typically seen as the formation of a wake behind the object, and this kind of drag is less sensitive to Reynolds number than frictional drag. It is also called form drag.

In both cases of drag, it is generated because of viscosity in the fluid[19]. Theoretically, objects moving through an inviscid fluid would create no drag.

### 2.3.3 Streamlined or bluff objects

When viscous drag is the dominant drag, we say that the object is streamlined. When pressure drag is the dominant drag, we say that the object is bluff. Cylinders and spheres are considered bluff bodies because at large Reynolds numbers pressure drag is the dominant drag force.

When fluid is flowing over a bluff body, it will accelerate and create a pressure drop. Along the surface, the flow will eventually expand and decelerate which will increase the pressure. This difference in pressure will cause the downstream flow to reverse direction. The upstream flow has some momentum, but due to viscous friction and the fact that the downstream flow is reversed, it will separate. See figure 2.2.

The separated flow will increase drag and the size of the wake, so what we want is to delay the separation. A turbulent boundary layer is more persistent

to adverse pressure gradients than a laminar boundary layer, which is why it is favorable to make the flow around the body transition to turbulent as soon as possible. The momentum of the turbulent boundary layer is higher and can withstand the force from the reversed flow longer.

### 2.3.4 Bodies with sharp edges

In the case of smooth bodies with rounded shapes, the Reynolds number influences the nature of the flow significantly. This means that when we are using models in the wind tunnel, the Reynolds number is an important factor for e.g. platform legs and tower framework. For bodies with sharp edges, for example rectangular shapes like the platform deck and other details, the flow will be forced to separate at the sharp edges. This will happen both in the wind tunnel and at full-scale, which means that it is Reynolds number independent, thus less important to consider.

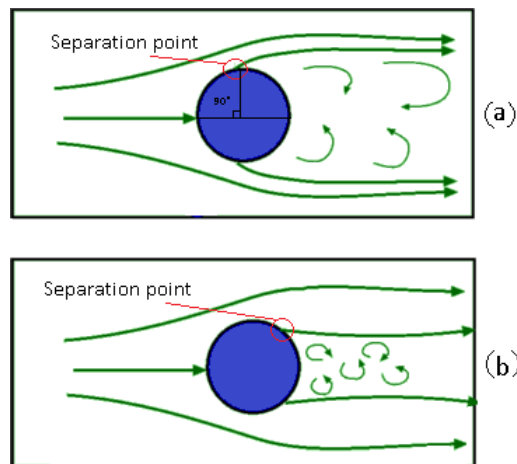


Figure 2.2: Boundary layer separation  
<http://artvb.oatmeal.dhs.org/images/54.gif>

### 2.3.5 Transition from laminar to turbulent boundary layer and flow separation

At lower Reynolds numbers ( $\sim Re \leq 10^5$ ), the boundary layer at the front of the cylinder is laminar. Flow separation occurs almost immediately as the pressure gradient becomes adverse which is at approximately  $90^\circ$  (see (a) in figure 2.2), with a subsequent large wake and increased total drag. At higher Reynolds numbers ( $\sim Re \geq 10^6$ ), the boundary layer becomes turbulent.

Flow separation is delayed and happens at a later stage (see (b) in figure 2.2). The following wake is significantly smaller and the total drag should go

down as well. It follows that, if we can make the boundary layer turbulent at a lower Reynolds number, the drag will go down.

Experiments will be conducted to induce the transition to a turbulent boundary layer at a lower Reynolds number by changing the surface roughness of the cylinder by applying a coat of sand (see section 4.3.3). There are also other parameters to consider that influence the flow around the body, such as aspect ratio, oscillations, turbulence in the free stream and boundaries in the test area i.e. wall interference.

## 2.4 Reynolds number vs drag coefficient

The correlation between the drag coefficient and its corresponding Reynolds number is an effective way of figuring out where the flow goes from laminar to turbulent flow. We want to be able to conduct the experiments with the model platform so that the flow around e.g. the cylindrical legs is in the turbulent range with the generated wind tunnel velocity, since we can assume that at full-scale the boundary layer on the cylinder is predominantly or fully turbulent. As seen in section 2.2.1, we get a correlation between the drag coefficient and the Reynolds number, both values non-dimensional.

In figure 2.3, it shows a typical  $C_D - Re$ -graph. As the Reynolds number increases,  $C_D$  decreases, drops and increases again. The drop is not fixed to a certain Reynolds number, but depends on the shape and surface roughness of the body, and it is unstable because of the turbulence surrounding the body.

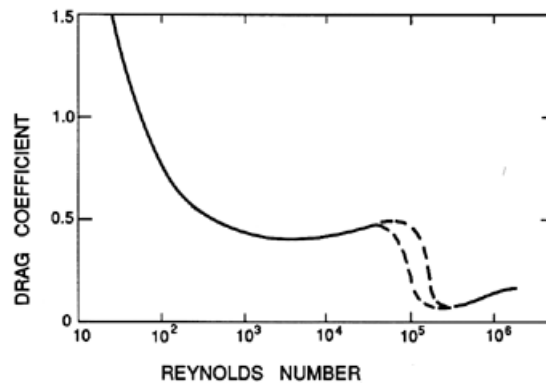


Figure 2.3: Typical  $C_D - Re$  graph for a circular cylinder

<http://authors.library.caltech.edu/25017/4/figs/fig503.gif>

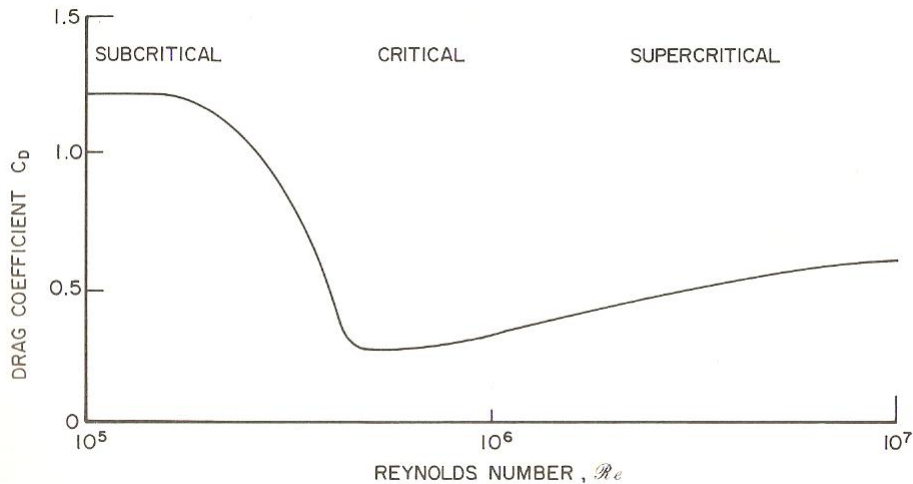


Figure 2.4: Critical region

From L.R. Wooton and C. Scruton, “Aerodynamic Stability”, in ‘The Modern Design of Wind-Sensitive Structures’, Construction Industry Research and Information Association, London, UK, 191

### 2.4.1 Critical region

As we can see from figure 2.4, there is a drop in drag at a certain Reynolds number (approximately  $4 \cdot 10^5 \leq Re \leq 6 \cdot 10^5$ ). This is the critical region, where the boundary layer around the body transitions from laminar to turbulent flow, explained in section 2.3.5. The turbulent mixing that takes place in the boundary layer gives the fluid a higher momentum toward the surface of the body, thus moving the separation point farther back. In the critical range, small variations in the Reynolds number cause considerable changes in the drag coefficient.

After the drop and as the Reynolds number increases further, we move into the supercritical region, where  $C_D$  increases again, but it stays lower than it was in the subcritical region. Increasing the Reynolds number further would lead into the transcritical range where the flow almost immediately transitions from laminar to turbulent. In the transcritical range, the drag coefficient is nearly independent of the Reynolds number. Little experimental data is found on this subject, but some information is presented by Achenbach [2], where it seems that the drag coefficient stabilizes for Reynolds number beyond  $10^6$ .

As mentioned earlier, we want to shift the place where the drag coefficient drops to a lower Reynolds number. As we can see from figure 2.5, from earlier experiments by White [19], with  $k = \textit{grain size}$ ,  $r = \textit{corner radius}$ ,  $h = \textit{diameter}$ , by varying the surface roughness of the cylinder, we can cause an earlier transition to a turbulent boundary layer.



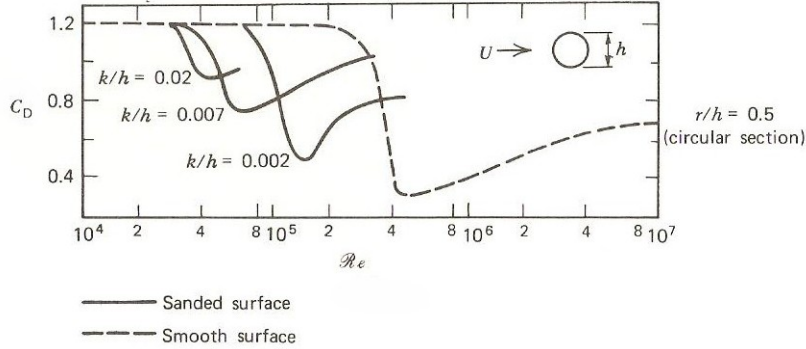


Figure 2.5: Surface roughness[16]

### 2.4.2 Surface roughness

Surface roughness is based on a relative roughness  $\frac{k}{h}$  (as seen in figure 2.5) and shows the size of the roughness elements divided by cylinder diameter. We can observe that with a rough surface, the drop in  $C_D$  happens sooner, but the amplitude of the drop is smaller. The value of  $C_D$  in the transcritical region is higher for the cases with a rough surface than the smooth case.

It is suggested by Gandemer, Barnaud and Bietry [12], that the thickness  $k$  of the roughness elements should satisfy the relations to maintain accurate flow conditions:

$$\text{Roughness Reynolds number: } \frac{Vk}{\nu} \geq 400 \quad (2.26)$$

$$\text{Relative roughness: } \frac{k}{h} \leq 10^{-2} \quad (2.27)$$

## 2.5 Atmospheric boundary layer

The interaction between the wind and earth or sea in the lowest part of the atmosphere creates a flow field which is not uniform, depending on several parameter such as surface roughness and friction, the Coriolis effect and thermal properties of the air. The earth's surface creates a horizontal drag force which causes the wind to retard. The effect is diffused by turbulent mixing throughout the region known as the atmospheric boundary layer. Within this layer, the wind velocity increases with height until it reaches its maximum velocity, sometimes known as the free-stream velocity (see figure 2.7), where the surface no longer has any influence on the wind speed. The velocity profile depends on the type of terrain, as we can see in figure 2.6.

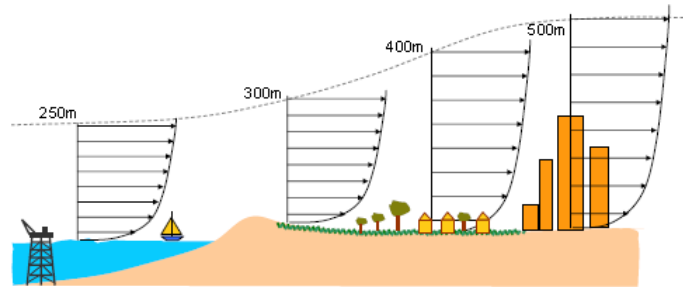


Figure 2.6: Illustrative velocity profiles for different types of terrain

<http://www.ejse.org/Archives/Fulltext/2007/Special/200705.pdf>

The turbulence is mainly a product of thermal and mechanical turbulence. Thermal turbulence occurs when columns of air, warmed by the surface, rises and meets with falling, colder air higher in the atmosphere causing it to break into eddies. Thermal turbulence depends on the time of day, as it is a function of surface temperature and heating from the sun. Mechanical turbulence is caused by motion of air being disrupted by roughness in the terrain e.g. hills, houses, vegetation. This is the kind of turbulence that we provoke when we want to simulate an adiabatic atmospheric boundary layer in the wind tunnel e.g. use of spires, barriers or blocks upstream of the model.

According to Plate [9], there are two main reasons for simulating an atmospheric boundary layer in the wind tunnel. One is to help with the understanding of airflow in the atmosphere as a combined effort between engineers and meteorologists. The other is to be able to solve problems such as; predicting wind forces on structures and predict how the structure affect airflow on other objects around it. Another area of interest could be accumulation of sand or other objects around buildings.

There are a few important requirements that need to be correct to get as good as possible simulated natural atmospheric boundary layer. These are presented by Cermak [9], and are 'similarity of relative surface roughness', 'simulation of boundary layer velocity distribution and turbulence intensity', 'matching of Reynolds number, Rossby number [ratio of inertial to Coriolis force: relates shear forces to forces from the Coriolis acceleration] and Richardson number [ratio of potential and kinetic energy of the flow]' and 'matching the zero pressure gradient as in real-life'.

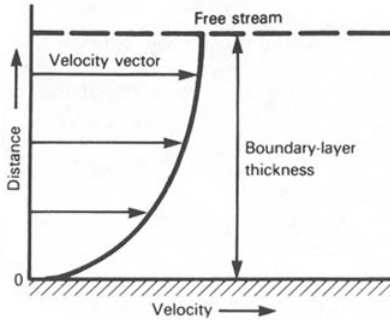


Figure 2.7: Velocity profile within boundary layer

<http://history.nasa.gov/SP-4103/app-f.htm> &

### 2.5.1 Boundary layer profile

The air flow in the atmospheric boundary layer can be categorized into the 'main flow' and the 'boundary layer flow' [18]. In the main flow, fluid friction is negligible and in the boundary layer, fluid friction is the main component. The boundary layer within a wind tunnel is supposed to simulate the same turbulent characteristics found in the full-scale atmospheric boundary layer, which is especially important by the model. Otherwise, local velocity changes over the model will not be simulated correctly and the results will be inaccurate.

There are four types of terrain related to the defining of the structure of the atmospheric boundary layer: smooth (ice, mud, snow, sea), moderately rough (short grass, grass/crops, rural), rough (rural/wood, woods, suburbs) and very rough (urban). They all have different characteristic parameters so that we will be able to simulate the boundary layer properly, regarding turbulence intensity, roughness length and power law exponent. Tabulated values may vary between sources, but all in all the values are in good agreement.

Two types of wind profile laws are typically used today to describe the atmospheric boundary layer, and that is the theoretically derived logarithmic profile and the empirically derived power law, where the power law is widely used for its simplicity. According to Emeis [8], the power law offers a good fit to the logarithmic profile for slightly stable conditions and very smooth surfaces only, which means it is a good fit of the wind profile over the sea, but not so much over rough terrain.

The logarithmic velocity profile is, with  $V$  = velocity at height  $z$ ,  $V_*$  = shear velocity as a function of shear stress and air density,  $\kappa$  = von Karman constant=0.4,  $z_0$  = aerodynamic roughness length:

$$\frac{V}{V_*} = \frac{1}{\kappa} \cdot \ln \left( \frac{z}{z_0} \right) \quad (2.28)$$

More commonly is the power law, (which is a general form of equation 2.1), where  $V$  = velocity at height  $z$ ,  $V_\delta$  = velocity at reference height  $\delta$ :

$$\frac{V}{V_\delta} = \left(\frac{z}{\delta}\right)^\alpha \quad (2.29)$$

The empirical exponent  $\alpha$  defines the shape of the velocity profile and is determined by the terrain roughness, which in the case of offshore tests in the open sea (smooth surface) means a low value of  $\alpha$ .

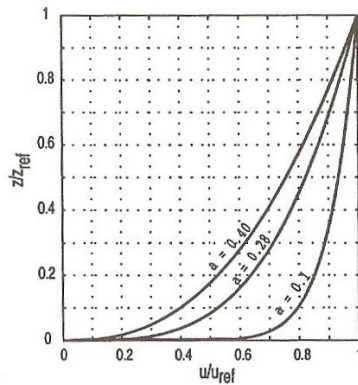


Figure 2.8: Boundary layer velocity profile based on the power law with different values of  $\alpha$ [13]

See figure 2.8 for some characteristic shapes of the power law with different values of  $\alpha$ . The value of  $\alpha$  in the wind tunnel must match the full-scale value if they are to be similar. To achieve similar  $\alpha$  in the wind tunnel, there are several different techniques that can be used:

- Long tunnels, where the boundary layer develops naturally along the rough floor
- Tunnels with active devices, like jets, machine-driven shutters or flaps
- Tunnels with passive devices, where a thick boundary layer is generated using grids, fences or spires placed at the entrance of the test section, combined with other roughness elements at the floor, such as a wooden blocks or sticks

### 2.5.2 Theoretical design versus experimental design

The wind tunnel in the Aerodynamics Lab at NTNU uses passive devices to create the boundary layer. At the test section entrance, there are 5 equally spaced triangular spires, decreasing in frontal thickness linearly from the bottom to the ceiling. There is also a trip function, a lateral barrier, to further accelerate

generation of turbulence. Thermal influence is neglected. See illustration in figure 2.9 (the spires used by NTNU are in reality at height with the tunnel,  $h = H$ ) and values in table 2.2.

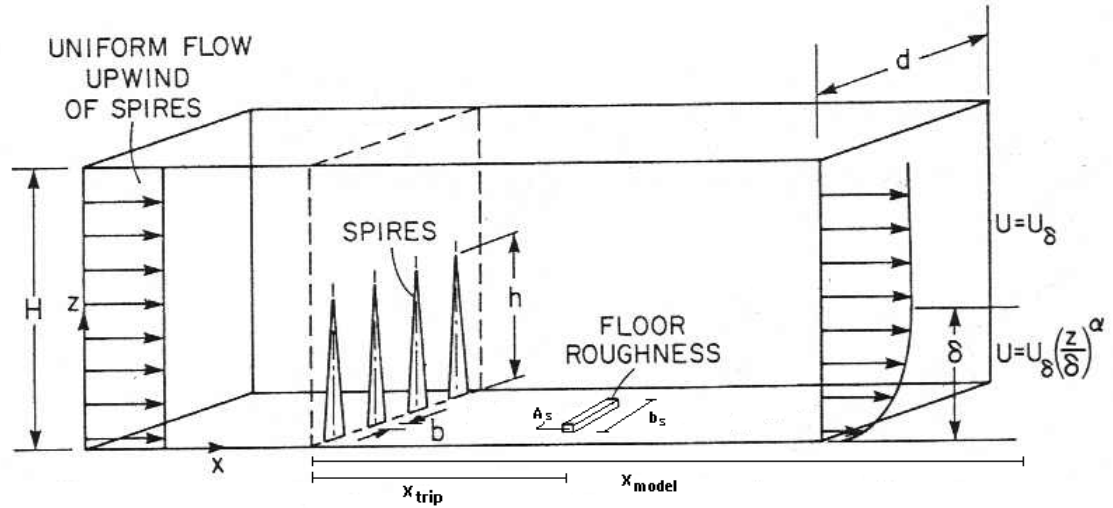


Figure 2.9: Atmospheric boundary layer set-up in the wind tunnel

<http://www.idr.upm.es/aerodinamica/proyecto/biblio/Wei%20&%20Desmond,%20internal%20report.pdf>  
(modified)

Variable	NTNU [cm]
$H$	180
$d$	271
$h$	180
$b$	13.7
$b_{centerline}$	57.5
$A_s$	3.3
$b_s$	203
$x_{trip}$	206
$x_{model}$	421
$x_H$	2.3
$\alpha$	0.11-0.14
$\delta$	unknown

Table 2.2: Spire and barrier dimensions at NTNU

The boundary layer set-up has been designed according to experimentation (trial-and-error) and validated based on measurements of the velocity profile and turbulence intensity, which will be addresses later on. In the case of knowing

the desired boundary layer height, it is possible to use the following theoretical assumptions.

Theoretical spire design: It is assumed that the flow upstream of the spires is uniform, and that the boundary layer generated downstream should resemble the power law velocity profile. The appropriate design of the spires is discussed by Irwin ([11]), and he shows that with the right height, width and distance between spires, a boundary layer is generated at approximately 6 times the height of the individual spire downstream of the spire array. At that distance, lateral uniformity is supposedly ensured. The distance between the centerline of the spires should be around half of the height,  $\frac{h}{2}$ . The expression for the height of the spires  $h$  as a function of boundary layer height  $\delta$  and values of  $\alpha$  is:

$$h = \frac{1.39 \cdot \delta}{1 + \frac{\alpha}{2}} \quad (2.30)$$

There is also an expression for the ratio between spire height  $h$  and base width  $b$  as suggested by Irwin ([11]) (re-reference from [14]):

$$\frac{b}{h} = \frac{\psi}{2} \cdot \frac{H}{\delta(1 + \psi)} \cdot \left(1 + \frac{\alpha}{2}\right) \quad (2.31)$$

where

$$\psi = \beta \cdot \frac{\left[ \frac{2}{(1+\alpha)} + \beta - \frac{x_H}{6} \cdot \frac{1.13\alpha}{(1+\alpha)(1+\frac{\alpha}{2})} \right]}{(1 - \beta)^2} \quad (2.32)$$

and

$$\beta = \frac{\frac{\delta}{H} \cdot \alpha}{(1 + \alpha)} \quad (2.33)$$

where  $H$  is the height of the wind tunnel, and  $x_H$  is the distance to the desired boundary layer simulation location as a factor of spire height  $h$ . In general,  $x_H = 6$  times the height  $h$ . In our case, the distance is approximately 2.3. Equation 2.31 relies on roughness elements along the floor of the tunnel explained in 'theoretical roughness element design' paragraph.

Theoretical roughness element design: Rough flow is when shear stress is dominated by drag of the roughness elements, as smooth flow is where shear stress is dominated by viscosity. The role of the surface roughness is to act as a momentum sink, controlling the mean velocity profile and turbulence. We want to generate rough flow with sufficient turbulence near the floor surface. If we were to use roughness elements along the floor, cubes, with side  $k$  and spacing  $D$  between them, this empirical equation is used [20]:

$$\frac{k}{\delta} = \exp \left[ \frac{2}{3} \cdot \log \left( \frac{D}{\delta} \right) - 0.1161 \left[ \frac{2}{C_f} + 2.05 \right]^{0.5} \right] \quad (2.34)$$

where  $C_f$  is a friction coefficient using the  $\alpha$  from the power law:

$$C_f = 0.136 \left( \frac{\alpha}{1 + \alpha} \right)^2 \quad (2.35)$$

It should be noted that the theoretical design is just a guideline and can be helpful in the case of knowing the desired boundary layer height. With a model scale of 1:150, it is difficult to simulate the whole boundary layer height, which means we focus on simulating the lower part of the atmospheric boundary layer. The best measure of accuracy is to measure the velocity profile experimentally to see if it is correct, see figure 2.10. There is no 'right' answer to the set-up, especially since the shape of the velocity profile is mainly the design condition (i.e. power law) instead of the boundary layer height.

At NTNU, a barrier has been used with distance  $x_{trip}$  from the spire array. Using a pitot tube at the test section to measure velocity, it is possible to validate the accuracy of the generated boundary layer and get the required likeness to the theoretical power law. Using equation 2.1 with  $\alpha$  equal to 0.11 and 0.13 (values based on earlier velocity profile measurements, which is in accordance with NMD-regulations), we get the profiles shown in figure 2.10. As we can see, the generated velocity profile is almost identical to the theoretical profile with the corresponding  $\alpha$ -values shows as 'measured values'. Thus, we assume that the simulated boundary layer is adequate for experiments.

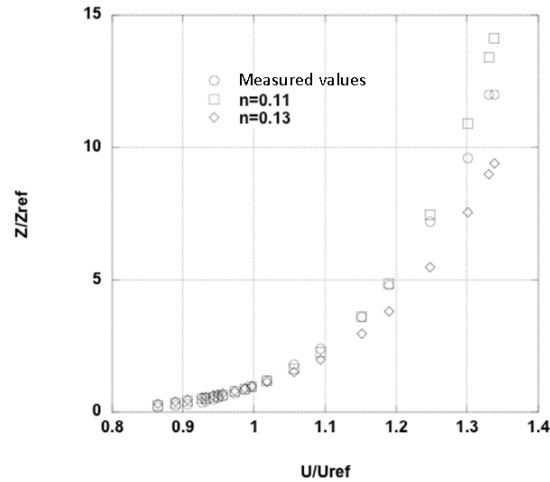


Figure 2.10: Theoretical versus experimental wind velocity profile

### 2.5.3 Turbulence intensity

Another important parameter to consider when simulating an atmospheric boundary layer is the turbulence intensity, which is the ratio of the standard deviation

of the fluctuating wind to the mean wind velocity. The rate of generation of turbulence and its intensity is a function of the Reynolds stresses and the mean velocity profile. Turbulence is generated by eddies due to shear stress which causes fluctuations in velocity. The stronger the shear, the stronger the turbulence. Turbulence is strongest close to the boundary and decreases with distance. We can decompose the velocity as follows (Reynolds' decomposition):

$$u_i = U + u'_i \quad (2.36)$$

where  $U$  is the mean and  $u'$  is the turbulent fluctuation component.

The root mean square velocity fluctuation, with  $n$  = sample size, at a given point is given by:

$$u' = \sqrt{\sum_{i=1}^n \frac{(u_i - U)^2}{(n - 1)}} \quad (2.37)$$

The relative turbulence intensity which indicates the total energy of the flow residing in the turbulent regime is estimated with:

$$I_u = \frac{u'}{U} \quad (2.38)$$

All three equations with  $u$  (longitudinal) applies to  $v$  (lateral) and  $w$  (vertical) too. A turbulence intensity of 1% is considered low and turbulence intensities higher than 10% are considered high. According to Counihan [6], the turbulence intensity  $I_u$  when  $z = z_{ref}$  should be close to the numerical value of  $\alpha$  (see equation 2.39). If we look at the test results for the simulated atmospheric boundary layer at NTNU done earlier (figure 2.11), we see that  $I_u(z_{ref}) \approx 0.11$ , which is acceptable. Usually,  $z_{ref}$  is set to be at 30 m based on the fact that measurements should be free from very local influences. In our case it is 10 m by NMD regulations, but if we look at  $\frac{z}{z_{ref}} = 3$ , the turbulence intensity is even closer to the value 0.11.

$$\frac{u'}{U} = \frac{1}{\ln\left(\frac{z}{z_0}\right)} = \alpha \quad (2.39)$$



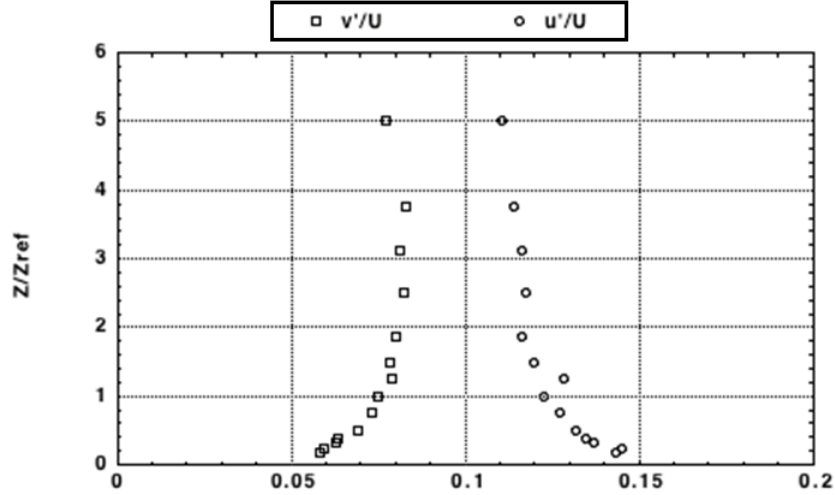


Figure 2.11: Turbulence intensity experimental results

What we do not see in the results, is that close to the floor there is a thin region called the laminar sub-layer where there is no turbulence. This is because of the no-slip condition, where the velocity of the fluid is the same as the boundary velocity i.e. the floor. The sub-layer thickness decreases with increased turbulence levels and higher velocities. In our case, this layer is very small.

### 2.5.4 Wind spectrum

The wind spectrum describes the frequency of wind variations, which causes velocity fluctuations and contributes to generation of turbulent flow. The most important turbulence component is the longitudinal component  $u(t)$  and the most common spectrum is the von Karman spectrum:

$$\frac{f S_u(f)}{u_*^2} = \frac{4 \left( \frac{f L_x}{U} \right)}{\left( 1 + 70.8 \left( \frac{f L_x}{U} \right)^2 \right)^{5/6}} \quad (2.40)$$

where  $f$  is the frequency,  $S_u$  is the energy spectrum of the longitudinal velocity component  $u$ ,  $u_*^2$  is its variance and  $L_x$  is the integral length scale of turbulence.

Experimental results are presented in figure 2.12, where the x-axis is a non-dimensional length scale  $X^*$  defined as  $\frac{f L_x}{U}$ . The integral scale obtained was  $L_x = 26$  m (full-scale). The blue line shows the recommended spectrum by ESDU (1987). The measured values for the simulated boundary layer matches

the recommended values fairly good, which indicates that the dynamics of the flow field is properly simulated with the correct decay of the length scale of turbulence.

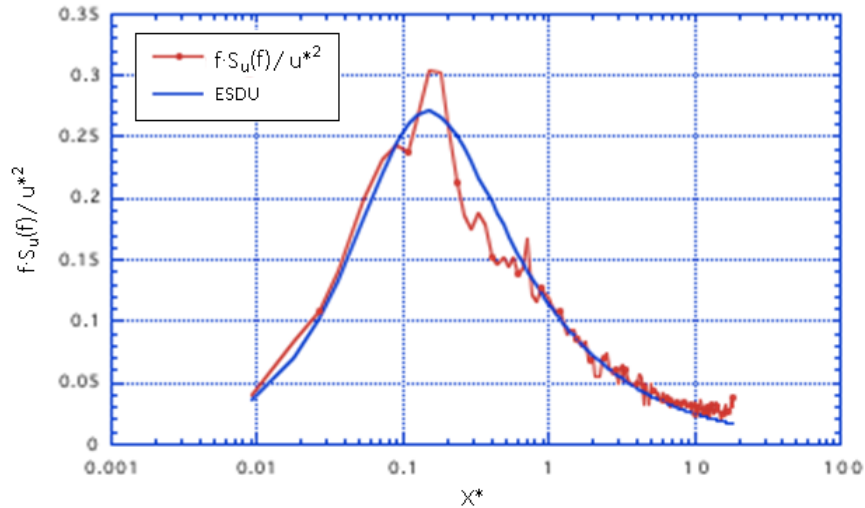


Figure 2.12: Wind spectrum at  $z = 30$  m

### 2.5.5 Limitations

At a conference in 1974 discussing atmospheric boundary layers in wind tunnels, V. Nee [9] claimed that passive devices was inadequate for simulation of turbulence intensities, as passive devices creates turbulence from kinetic energy of the mean flow, meaning that the mean velocity profile and turbulence are not independently variable. With active devices, it is easier to control and the mean velocity of the flow would be independent of the turbulence created by the devices.

According to Simiu [17], there are four problems connected to creating an atmospheric boundary layer in a wind tunnel:

- Flow simulation in the wind tunnel is affected by the violation of the Reynolds number (i.e. it is impossible to recreate correct Reynolds number conditions in a wind tunnel, see section 2.2.2)
- Atmospheric boundary layer flows develops by friction over long distances at earth’s surface, whereas flow in a wind tunnel often travels short distances and may not be able to reproduce the correct turbulence scales relative to the model
- Due to the rotation of the earth (the Coriolis effect), the flow is subject to veering, which is significant for tall objects (see figure 2.13). This is not

reproduced in the wind tunnel

- Wind is not constant or regular (as with surface temperature), which means that in reality, the velocity profile differs with time

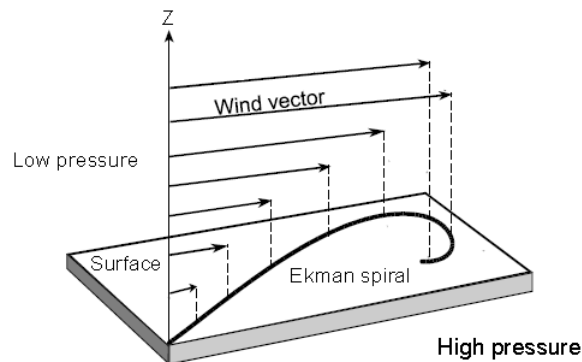


Figure 2.13: Ekman spiral of wind

## 2.6 Wind tunnel blockage

The problem of blockage is of great concern when doing wind tunnel experiments and it is one of the main error sources. Because of the walls of the wind tunnel, the flow around the model acts differently than it would at free stream.

The wind tunnel at NTNU is a closed-section tunnel, which means that a model in the test section will make the flow area smaller. The presence of the wind tunnel walls increases the measured forces and moments. The effects upon the flow over a model is divided into four different types, the first two most relevant[3]:

- Solid blockage: an increase in free-stream velocity around the model caused by constriction of the flow. This depends on the volume and shape of the object. Given that the reduction of the cross-section area is smaller past the test section with the model in place, velocity has to increase past the model because of the law of continuity and Bernoulli's equation. We have to consider this when calculating coefficients, as it affects all forces and moments.
- Wake blockage: blockage because the wake of the model is not able to develop naturally because of wall constraints. Velocity within the wake is lower than the freestream velocity, which means that the flow around the model will have to increase to satisfy the continuity equation. Compared to solid blockage, where the increase in velocity is temporary past the model, wake blockage causes an increase in velocity from the model and beyond (see illustration in figure 2.14). It affects primarily the drag force.

- Streamline curvature: the normal curvature of the free air-flow about a model is straightened by the tunnel walls so it appears to have more camber than it actually has. This means that we measure too much lift.
- Buoyancy: the boundary layer grows on the walls of the wind tunnel and becomes equivalent to a contraction in the working section. The flow is accelerated, causing a drop in static pressure. This means that models with a large frontal area are pushed backwards and artificially increases drag.

To know exactly to what degree the various corrections apply to each force and moment is hard to tell, as they are affected differently. The methods in the following sections focus primarily on the effect on drag.

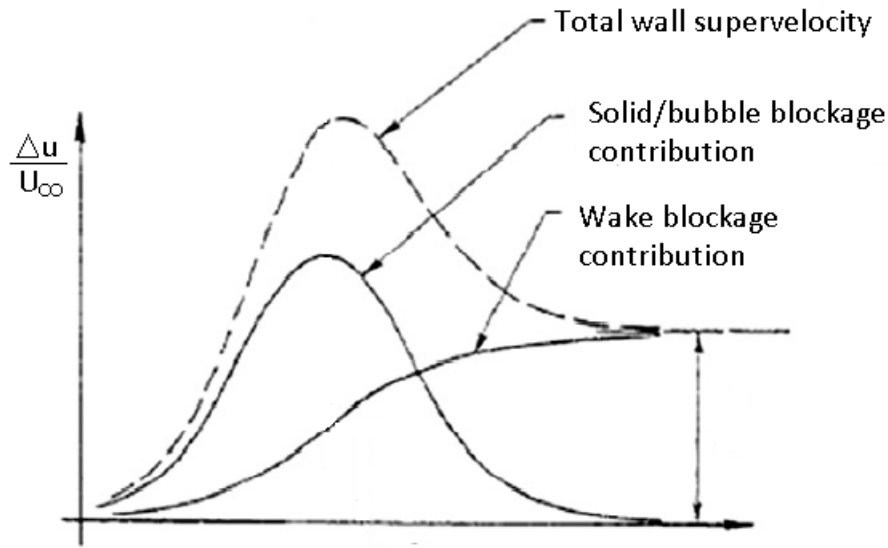


Figure 2.14: Increase in velocity due to solid and wake blockage[10]

The ideal test environment is for the flow around the test object to resemble the flow in free air completely. Since this is impossible, we have to look at a way to compensate for the wind tunnel wall interference with the flow. If we look at this simplistically, we can make an easy equation for the increase in velocity around the model by using mass conservation,  $\dot{m} = \rho AV = \text{constant}$ , where density is considered constant throughout the wind tunnel:

$$V_c \cdot (S - A) = V_{measured} \cdot S \quad (2.41)$$

where  $V_c$  means velocity passed the model area  $S$ , which gives us this equation for the corrected drag coefficient:

$$C_{Dc} = C_D \cdot \left( \frac{(S - A)}{S} \right)^2 \quad (2.42)$$

However, this is not totally accurate, as there are several blockage effects to consider, such as the effect of wake and wake displacement. Therefore, we have to account for the combined blockage from both solid and wake blockage, which we will call total blockage.

Since bluff bodies are inefficient generators of lift, there has been a minimal study of the correction of forces normal to the flow direction.

At the Aerodynamics Lab at NTNU, they have operated with this blockage correction for the measured forces:

$$\frac{F_c}{F_m} = 1 - \left\{ \frac{\sin}{\cos} \right\} |\theta| \cdot k \frac{S}{A} \quad (2.43)$$

where the subnote c means corrected, m means measured,  $\theta$  is the absolute value of the rotated angle from the zero angle, S is the wake area of the model, A is the wind tunnel cross-sectional area and k is a constant used by NTNU as 2.84, which might come from Maskell's method which is explained in section 2.6.2.

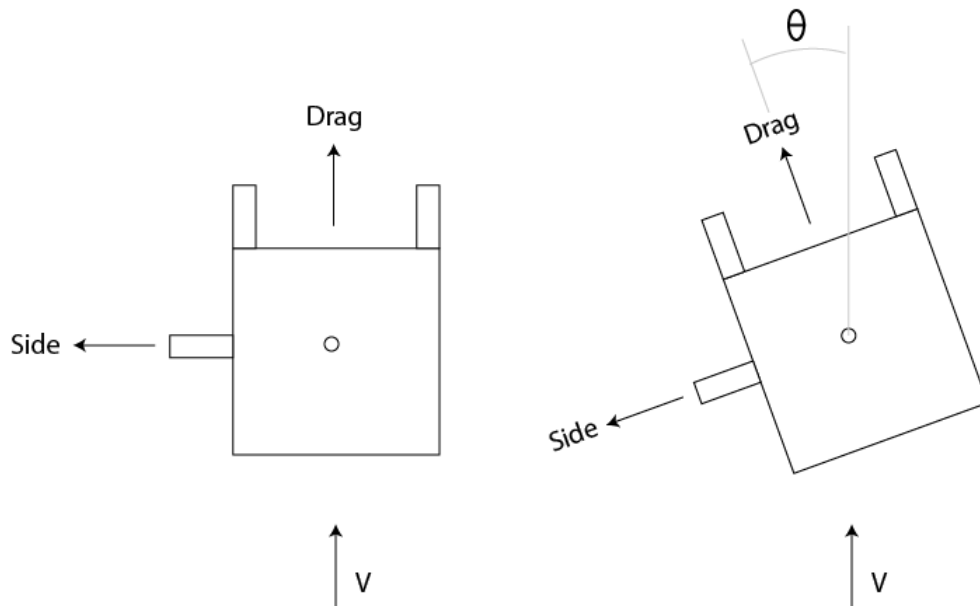


Figure 2.15: Zero angle and rotation illustration of model

Since the correction only applies to the drag force, we have to make an equation that depends on how the platform is rotated compared to starting position and how the forces are measured by the six component balance. As we can see from figure 2.15, when the balance is aligned the same way<sup>1</sup>, the following equations apply:

$$\frac{F_{sc}}{F_{sm}} = 1 - \sin|\theta| \cdot k \frac{S}{A} \quad (2.44)$$

$$\frac{F_{dc}}{F_{dm}} = 1 - \cos|\theta| \cdot k \frac{S}{A} \quad (2.45)$$

It is defined that total blockage is a combination of solid blockage and wake blockage, and it leads to an increment in velocity. A presentation of different methodologies and theories concerning wind tunnel blockage will be presented and the different corrections will be illustrated on the results from the offshore platform tests as a comparison. It should be noted that this is an area that still contains a lot of uncertainties, and that it is even more difficult to calculate with three-dimensional models, especially with a lot of turbulence.

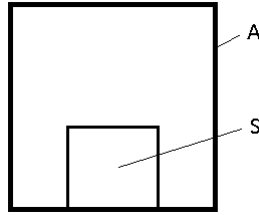


Figure 2.16: Blockage ratio

Solid blockage affects all forces and moments and can be applied to all coefficients by correction dynamic pressure or correcting coefficients later. It is then assumed that all forces and moments are equally influenced by the blockage, which is a practical assumption given that it is generally difficult to evaluate the blockage distribution.

Wake blockage primarily affects drag and is a special correction applied to drag. As it is difficult to know the correct blockage correction of moments seeing as they consist of a varying contribution quantity from lift, side and drag forces, in the following sections, a combined correction of solid and wake blockage will be applied to drag only. This is a simplification by the author.

<sup>1</sup>Alignment of the gages for drag is parallel to the wind velocity direction and the side force gage is perpendicular to the wind velocity direction

### 2.6.1 Pope and Harper

It is suggested by Pope and Harper that the projected area of a model should not be larger than 10% of the total cross-sectional area of the wind tunnel;  $\frac{S}{A} < 0,10$ .

From the book 'Low-speed wind tunnel testing' [13] by Pope and Harper, the following simplified corrections apply to all forces and moments:

$$\text{Velocity correction: } V = V_u(1 + \epsilon_t) \quad (2.46)$$

$$\text{Dynamic pressure correction: } q = q_u(1 + 2\epsilon_t) \quad (2.47)$$

$$\epsilon_t = \text{solidblockage} + \text{wakeblockage} = \epsilon_{sb} + \epsilon_{wb} \quad (2.48)$$

where  $\epsilon_t$  is the total blockage, combining solid and wake blockage. Pope explains: "for finding the blockage corrections for wind tunnel models of unusual shapes the following is suggested:"

$$\epsilon_t = \frac{1}{4} \cdot \frac{S}{A} \quad (2.49)$$

If we use equation 2.46 in combination with the relation 2.49 and that sub-  
notes m = measured and c = corrected, we can express the correction to the  
coefficients as:

$$\frac{C_m}{C_c} = \left(1 + \frac{1}{4} \cdot \frac{S}{A}\right)^2 \quad (2.50)$$

### 2.6.2 Maskell

The fundamental methodology for calculating wake blockage of bluff bodies in closed wind tunnels was that of Maskell. Maskell [5] shows that the dominant effect of blockage is an increase in the fluid's free-stream velocity, mainly determined by the shape of the body in solid blockage and displacement of the wake in wake blockage.

He used the results from tests with flat plates normal to the free-stream to determine a standard wall interference factor based on the increase in dynamic pressure. He based it on the momentum balance between the undisturbed flow upstream of the model to where the effective wake reaches its maximum width, B, downstream. The correction of force coefficients for models normal to the wind direction follows this relationship:

$$\frac{C_D}{C_{Dc}} = \frac{q}{q_c} = 1 + mC_D \cdot \frac{S}{A} \quad (2.51)$$

where m is an empirical constant determined by the drag and base pressure coefficient and the area-ratio. We call the term  $mC_D \cdot \frac{S}{A}$  for the blockage term.

According to the the paper of Ross Ian [10],  $m = \frac{B}{S}$ , where B is the wake area normal to the wind direction. This means that m is the factor between the area of the model and the size of the wake area.

If we look at figure B.1 in appendix B, suggested values of m are provided. We can see that for a rectangular block, where flow reattachment does not reoccur, values for flat plates should be used. With our estimation for the models A (figure 4.2) and B, with  $\frac{S}{A} \approx 0.10$ , the correction factors are valid. Since the model is mounted to the surface of the tunnel, these values apply:  $\epsilon = 2.37$  and  $m \approx 2.84$ . Remember,  $C_D$  is the coefficient of the drag contribution from the side and drag readings (see figure 2.15), and then use this equation:

$$\frac{C_D}{C_{Dc}} = 1 + 2.84 \cdot C_D \cdot \frac{S}{A} \quad (2.52)$$

$$\Rightarrow C_{Dc} = \frac{C_D}{1 + 2.84 \cdot C_D \cdot \frac{S}{A}} \quad (2.53)$$

### 2.6.3 Hackett

Hackett analyzed Maskell's blockage methodology and found that he tended to over-correct bluff-body drag data. The effective dynamic pressure correction that is found applies to change in dynamic pressure caused by tunnel interference, but also for incremental drag, that corrects for distortion of the separation bubble.

Maskell's correction applies to the separated-flow component of drag, which in the flat plate case is almost the total drag. In reality, some bluff bodies have other components to drag which means that Maskell's correction must be modified so that it only applies to the drag resulting from flow separation. Hackett made a two-step version of Maskell's method, where he combined the change caused by dynamic pressure with the change due to an increment in drag. The following equation presented in Coopers 'Bluff-body blockage corrections in closed- and open-test-section wind tunnels' represents the final solution [5].

$$\Delta C_D = \frac{C_{Dm}}{(1 + mC_{Dm} \cdot \frac{S}{A})} + \left[ \frac{1}{2m \cdot \frac{S}{A}} \right] \left[ 1 - \sqrt{1 + 4mC_{Dm} \cdot \frac{S}{A}} \right] \quad (2.54)$$

At large area-ratios, where Maskell's method have been seen to over-correct, the two-step Hackett method has been found to be better.

### 2.6.4 Comparison between methodologies

The calculated correction factors based on the different methodologies presented in previous sections is compared by applying them to the original data of model A with tower 2 (see 4.1). The only values included for the comparison is the side



force and the drag force. Mainly because the effect the correction has on the lift force, pitch, yaw and roll moment is uncertain, as they consist of unknown fractions of forces with different corrections applied to them.

As we can see from figure 2.17, there is little difference between the various correction methods of Pope and Hackett and the uncorrected data. The correction of Maskell lowers the values of side and drag forces more significantly, and it shows almost the same result as the method used by NTNU.

If we make a plot with the uncorrected values of  $C_D$  with the corrected values of the previously mentioned methods, it looks like figure 2.18. The highlighted area is the typical range of  $C_D$  based on values of earlier platform testing of model A and model B. We can see that within this range, the method of Maskell and the one used by NTNU is relatively similar. As predicted by Hackett, Maskell's method over-corrects at higher drag coefficient values.

It is difficult to know whether one method is better than the other without data from full-scale or model in free-flow to compare it with. It is apparent that, still today, there are a lot of uncertainties when it comes to correction of wind tunnel blockage. That means that we should at least, as suggested by Pope [13], keep the ratio between the model projected area and test section area ( $\frac{S}{A}$ ) below that of 10% to avoid faulty measurements even though we use corrections later.

## 2.7 Wind tunnel velocity

When calculating the Reynolds number and the drag coefficient, it is important to know the velocity of the moving fluid, in this case air. There are several different ways to measure the air velocity, two of them being using the venturi effect or using a pitot tube. The concept and the equations used in both cases will be explained in the following sections.

### 2.7.1 Venturi effect

The wind tunnel velocity is measured using an in-built venturi meter that measures static pressure at two different cross-sections. The total stagnation pressure remains constant, while the dynamic pressure changes, which means that the static pressure changes.

Based on the principles of the venturi effect, we can use the following equations to calculate the velocity.

$$p + \frac{1}{2}\rho V^2 + \rho g z = \text{constant} \quad (2.55)$$

$$\dot{m} = \rho Q = \rho A V \quad (2.56)$$

From the Bernoulli equation 2.55, we get that the velocity at the outlet of the wind tunnel,  $A_2$ , is:

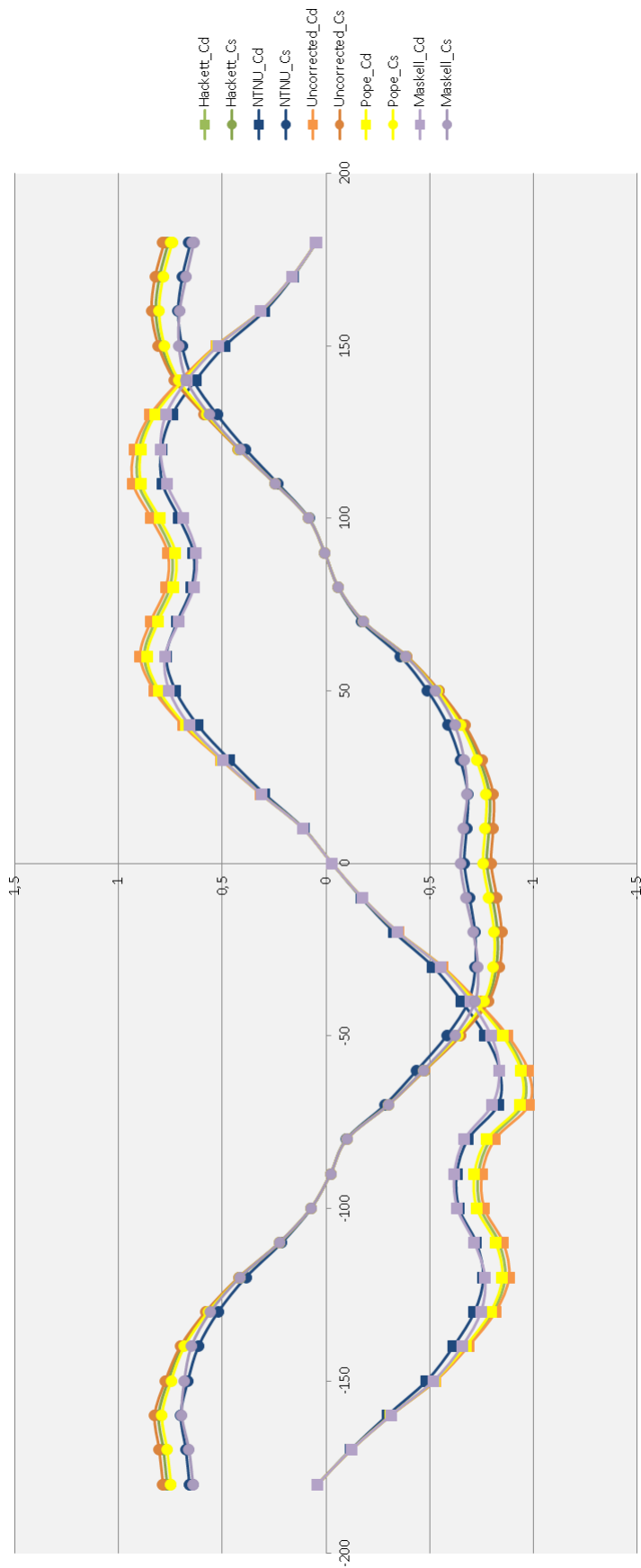


Figure 2.17: Data comparison of different correction methods

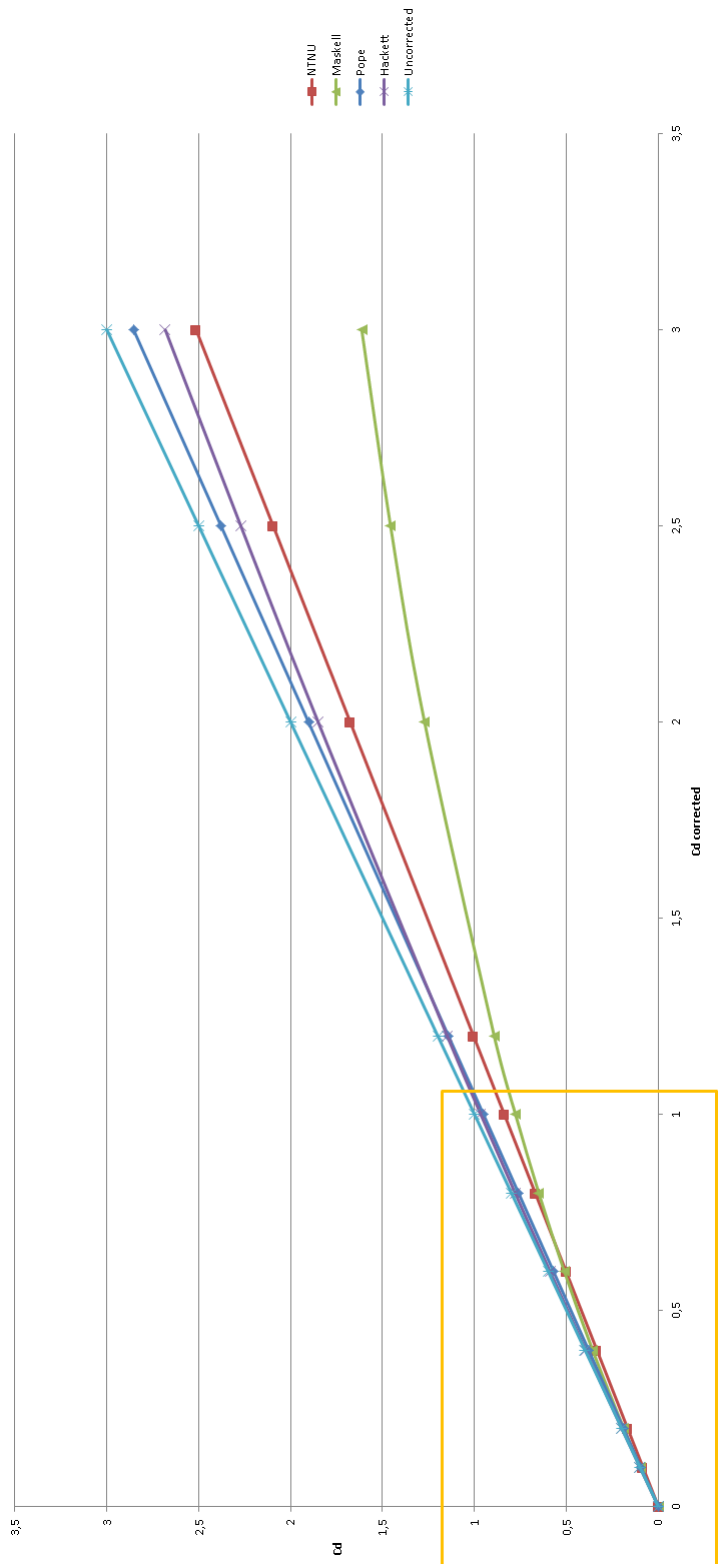


Figure 2.18: Comparison between methods for a range of values of  $C_D$

$$v_2 = \sqrt{v_1^2 + \frac{2\Delta p}{\rho_a}} \quad (2.57)$$

Since the density is the same for both areas  $A_1$  and  $A_2$ , we can simplify equation 2.56 into:

$$v_1 = v_2 \frac{A_2}{A_1} \quad (2.58)$$

If we combine equations 2.57 and 2.58, we get the pressure difference between  $A_1$  and  $A_2$  without the velocity in  $A_1$ .

$$\Delta p = \frac{\rho_a}{2} \left( v_2^2 - v_2^2 \left( \frac{A_2}{A_1} \right)^2 \right) \quad (2.59)$$

We want to obtain an equation for the velocity at the test section,  $A_2$ , which we will use in further calculations of the Reynolds number and the drag coefficient.

$$v_2 = \sqrt{\frac{2\Delta p}{\rho_a} \cdot \frac{1}{\left( 1 - \left( \frac{A_2}{A_1} \right)^2 \right)}} \quad (2.60)$$

The pressure difference  $\Delta p$  is calculated from data logging with the built-in Venturi meter at  $A_1$  and  $A_2$  using a pressure transducer. A manometer is used to calibrate the correlation between the data signal and pressure (explained further in section 3.8). The cross-section areas,  $A_1$  and  $A_2$ , are measured by hand with a measuring tape. The density of air  $\rho_a$  is measured using equation 2.61 and a mercury barometer (where  $\rho_{Hg} = 13534 \frac{kg}{m^3}$ ).

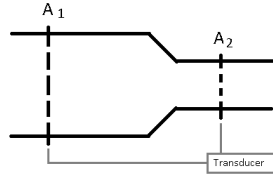


Figure 2.19: Wind tunnel cross-sections

It is reasonable to believe that the temperature inside the test area of the wind tunnel will change somewhat during the test period. Even so, to simplify, a constant density was used for the whole duration of the test which was measured just before each test was conducted.

$$\rho_a = \frac{p_a}{RT} = \frac{\rho_{Hg} \cdot gh}{RT} = 0.463 \frac{h}{(273 + T_r)} \quad (2.61)$$

where  $h$  = pressure read off the barometer in mm Hg,  $T_r$  = room temperature in  $^{\circ}C$

### 2.7.2 Pitot tube

The difference between the stagnation pressure and the static pressure (see figure 2.20) is called the dynamic pressure and can be used to calculate velocity. The equation for velocity as a function of the dynamic pressure is derived from the Bernoulli equation, considering that  $z_{static} = z_{stagnation}$  and  $v_{stagnation} = 0$ :

$$v_2 = v_{static} = \sqrt{\frac{2 \cdot (p_{stagnation} - p_{static})}{\rho_a}} = \sqrt{\frac{2\Delta p}{\rho_a}} \quad (2.62)$$

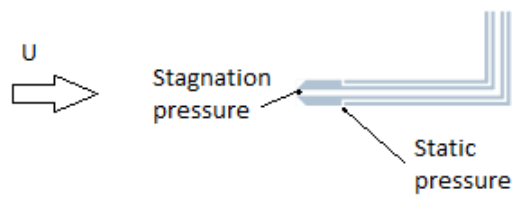


Figure 2.20: Pitot tube

## Chapter 3

# Experimental equipment

### 3.1 Wind tunnels

In the experiments, two different wind tunnels have been used at the Fluid Department lab at NTNU. For the testing of drag and skin friction of a circular cylinder, a small open-section wind tunnel, with dimensions at the test section being 1.06 m x 0.76 m was used. The maximum velocity is approximately 20 m/s. The test section has an opening at the bottom, which allows us to connect the model to a three-component balance for measuring.

For testing of the model platforms, model A and model B, a larger wind tunnel was used. It has a test section with dimensions of 2.7 m x 1.8 m x 11 m. The wind speed range is approximately 0-30 m/s, and it has a six-component balance to measure forces and moments. The test section with the connected balance consists of a circular section which can be rotated  $360^\circ$  in yaw to account for wind coming from every direction.

First, each component has to be calibrated, see section 3.3.1. From there, a test is conducted in the following order. When the tunnel is turned off and no air is passing through the test section, the weight of the model and mounting system is determined by the three gages located at R1, R2 and R3 (see figure 3.2). For every 10th degree, the zero point is recorded in LabView. The tunnel is then turned on and with air flowing over the model, aerodynamic forces and moments are generated that changes the readings of the strain gages. Again, for every 10th degree, the data is recorded. LabView uses the information from the zero point data to calculate the correct differential in voltage and thus data for the six different components. Forces and moments are to be presented as non-dimensional coefficients. Results are presented in chapter 4.

Name	Type of measurement
Lambrech Micro-manometer	Pressure difference
Lambrech Mercury barometer	Air pressure, temperature
National Instruments cDAQ-9172	Signal Converter
Schenck Six-Way Balance	Forces and moments
Crawley Sussex Three component balance	Forces and moments
Setra Pressure Transducer	Signal
Pitot tube	Dynamic pressure

Table 3.1: Instrumentation overview

## 3.2 Calibration and linearity

When doing the calibrations of the instruments for the experiment, it is important to check the linearity. We want the linearity to be as close to 1 as possible, because that means that the point values lie exactly in a straight line with minimal scatter (see figure 3.1). That means that if we know the value X, we can predict the value Y perfectly.  $y_i$ = measured value,  $\hat{y}_i$ = theoretical linear regression value,  $\bar{y}$ = mean value.

$$R^2 = 1 - \frac{SS_{err}}{SS_{tot}} = 1 - \frac{\sum_i (y_i - \hat{y}_i)^2}{\sum_i (y_i - \bar{y})^2} \quad (3.1)$$

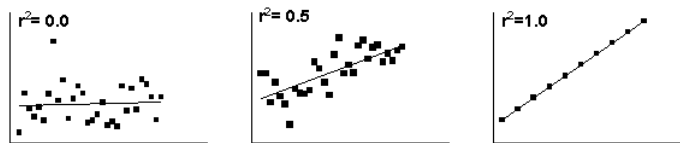


Figure 3.1: Linearity

[http://graphpad.com/curvefit/linear\\_regression.htm](http://graphpad.com/curvefit/linear_regression.htm)

## 3.3 Six-component balance

A six component balance is used to measure forces and moments on a model in the wind tunnel. The model is connected to the balance with bars through the test section floor. By measuring changes in voltage of the strain gages connected as shown in figure 3.2, we can measure lift force, drag force, side force, pitching moment, yawing moment and rolling moment ( $W$  = model weight). The coordinate system is fixed to the model and the charts are displayed accordingly, with the positive coordinate direction opposite of the side and drag force illustrated in the figure.

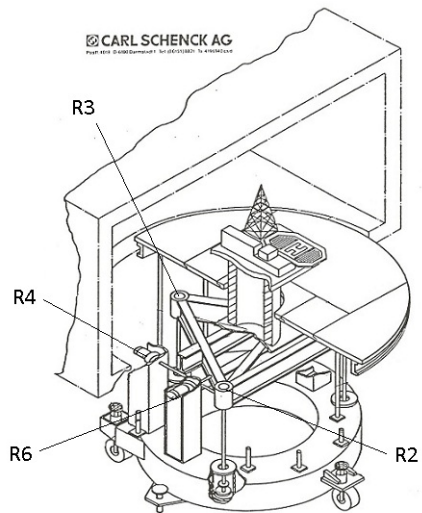
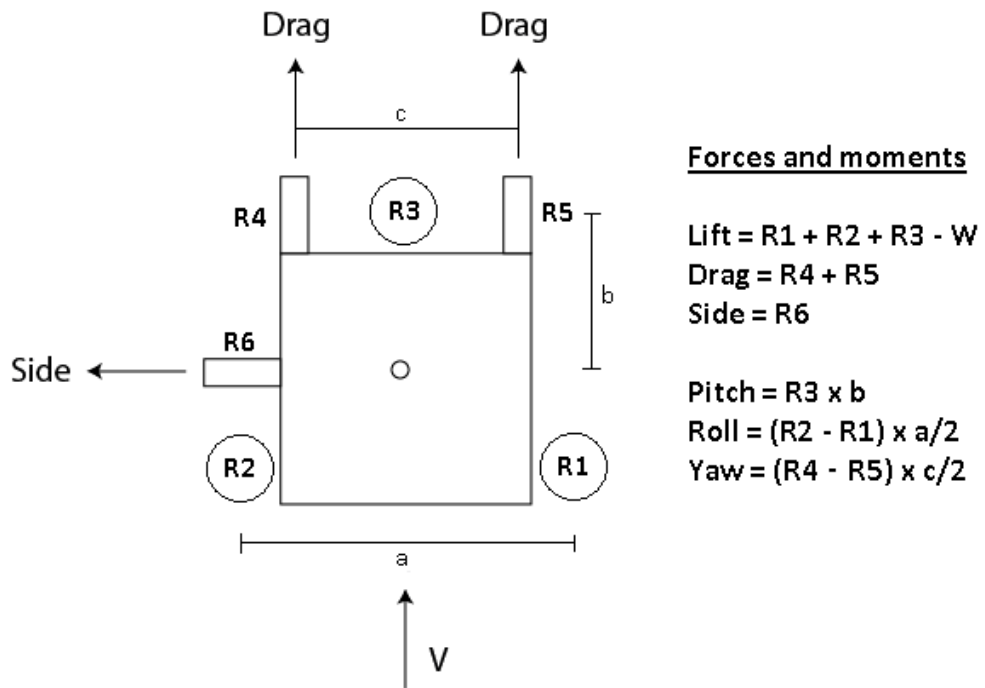


Figure 3.2: Overview of the set-up of the six component balance



### 3.3.1 Calibration

Calibration was done with all six components individually, by applying weights of 0.5, 1 and 2 kg and measuring the voltage output. A calibration factor was obtained for each component, which was multiplied by the gravitational constant to achieve Newton per voltage, N/V. These values were used to set-up the program in LabView before a test and made sure that all forces and moments could be calculated correctly based on voltage output. This was done prior to each test.

Component	Factor
R1	12,858 [N/V]
R2	5,917 [N/V]
R3	4,990 [N/V]
R4	6,756 [N/V]
R5	4,664 [N/V]
R6	6,181 [N/V]
R7 (velocity)	29,816 [Pa/V]

Table 3.2: Calibration factors R1-R7



Figure 3.3: Three-component balance weight beams

## 3.4 Three-component balance

The three component balance, Crawley Sussex, as shown in figure 3.4, measures drag, pitch and lift separately and independently with the possible exception

of lift interference on drag, due to the possibility of the four links not being vertical. This is prevented by aligning the earth frame correctly before start.

In the experiments, only the drag force will be measured. Drag is measured by using the weights on the beam to counter the force on the model (see figure 3.3) until it is level. Measured forces have to be multiplied by the gravitational constant to get Newton.

### 3.4.1 Calibration

The three component balance results are logged manually, which means it does not have a digital signal to be measured and logged via data. That means that drag is read directly. Mainly, the calibration consists of leveling the balance earth frame prior to each test. A table with calibration factors is included in the manual of the balance.

The validity of this is not certain, as these factors might be outdated, but they will be used in the experiments. Before testing, we have to make sure that the bubble level on the beam of the force we are to measure is level at 0 kg with the model mounted on the balance.

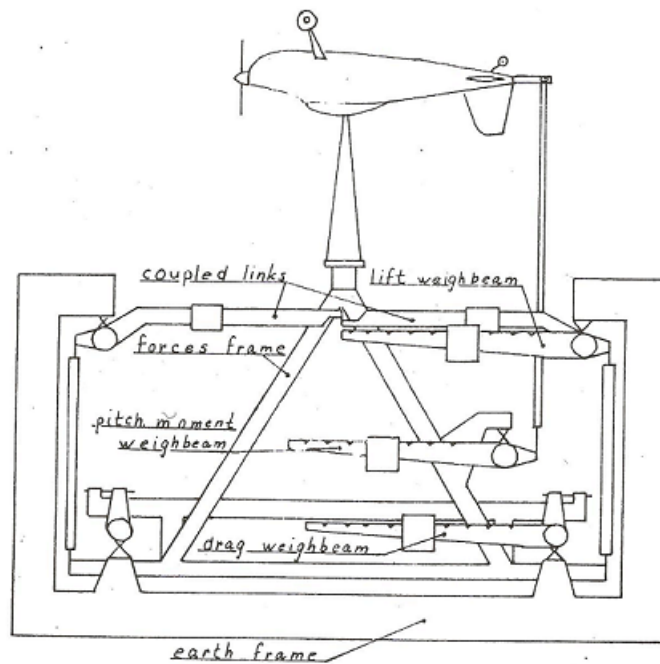


Figure 3.4: Three component balance

## 3.5 Venturi principle

In the wind tunnel, there are tubes that detect static pressure at two different cross-sections (see figure 2.19). By using the equations derived in section 2.7.1, we can calculate the velocity at cross-section  $A_2$  a.k.a. the test section. The static pressure difference is converted to an electric signal via a transducer and have to be calibrated using a manometer to find the correct gradient [Pa/V]. Calibration can be found in section 3.7.1.

## 3.6 Pitot tube

The pitot tube has an inner tube, measuring stagnation pressure, and an outer tube, measuring static pressure, as shown in figure 2.20. The tubes lead into a pressure transducer. Principle and equations are presented in section 2.7.2.

Calibration of the pitot tube signal comes from the transducer calibration, see section 3.7.1, since the calibration constant is independent of the measuring device/method used and applies to both the pitot tube and the in-built pressure differential.

## 3.7 Setra pressure transducer

In order to convert the measured dynamic pressure from either the pitot tube or the cross-section tubes in the tunnel into an electric signal for computer logging, we have to have a transducer. The voltage output from the transducer is proportional to the dynamic pressure from the pitot tube and from the in-built pressure differential, but it has to be calibrated with a manometer in order to find the correct gradient [Pa/V].

It is important to know that an amplifier was used for the calibrations, with gain=16. It means that the voltage signal received was amplified by a factor of 16, meaning  $V_{read} = 16 \cdot V_{measured}$ , making it easier to see smaller changes in voltage. When doing the actual experimental measurements, the same amplifying gain was used, which means that it was not necessary to account for it in the end results.

### 3.7.1 Calibration

From the graph in figure 3.5, we can see that the correlation is relatively linear, thus giving the relation between measured pressure difference (from manometer) and voltage output to be approximately  $\frac{\Delta p}{V} = 50.6 \frac{[Pa]}{[mV]}$ .

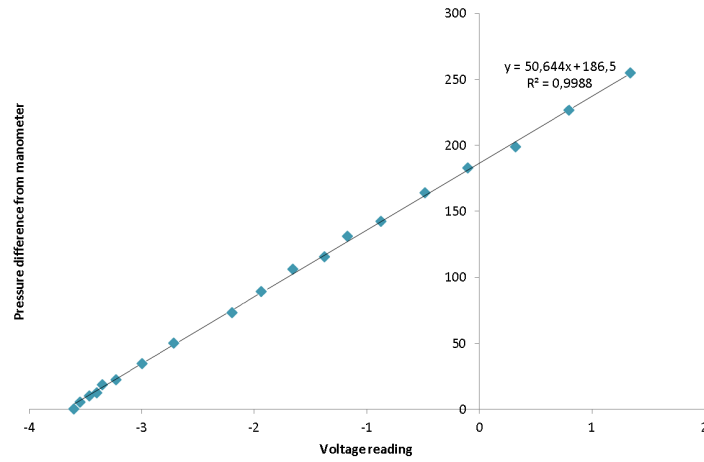


Figure 3.5: Calibration of transducer

### 3.8 Manometer

To check the correlation between the voltage, wind tunnel velocity and dynamic pressure, an inclined manometer was used. The liquid used is ethanol, with  $\rho_e = 789 \frac{kg}{m^3}$ .

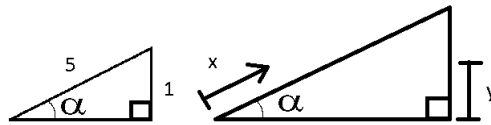


Figure 3.6: Manometer characteristics

The following equations refer to the sketch shown in figure 3.6.

$$\sin\alpha = \frac{1}{5} = 0.2 \quad (3.2)$$

$$\frac{y}{x} = \sin\alpha \Rightarrow y = 0.2 \cdot x \quad (3.3)$$

$$\Delta p = \rho_e g y \quad (3.4)$$

$$\Delta p = 789 \left[ \frac{kg}{m^3} \right] \cdot 9.81 \left[ \frac{m}{s^2} \right] \cdot y [m] = 1548.018x \left[ \frac{N}{m^2} \right] \quad (3.5)$$

This gives us the equation for the pressure difference as a function of  $x$  [mm], the length of the liquid column, as:

$$\Delta p \approx 1.548x \quad (3.6)$$

We will use equation 3.6 to calculate the pressure difference and insert into equation 2.60 to find the velocity at the test section.

### 3.9 National Instruments cDAQ-9172

The NI cDAQ-9172 is an eight-slot USB chassis designed for use with C Series I/O modules. It is capable of measuring a broad range of analog and digital I/O signals and sensors using a Hi-Speed USB 2.0 interface. We need to convert the analog signal from the transducer into a digital signal so that the computer can process it through the program LabView.

### 3.10 NI LabVIEW

LabView is a graphical programming environment used to log measurements, develop tests and control systems using a flowchart and an easy-to-understand user interface. It is compatible with a wide range of hardware devices, including NI USB, naturally, which is what we used for the experiment. This program allowed us to log several real-time data from our instruments, visualize the data and create mean values of selected sample sizes.

The values had to be within  $\pm 10V$  and the signals was amplified accordingly. All signals coming from the six-component balance had a starting value of circa 0 V, given that values would be both positive and negative depending on the rotational angle of the model. The voltage signal of measured velocity would be  $\sim -10V$ , as it would only increase. Amplification of each signal was determined beforehand.

## Chapter 4

# Experiments and results

When NTNU is conducting experiments with the model platform in the wind tunnel, it is important that the flow around the object is comparative with 'real' full-scale conditions.

The primary goal when testing the platform is to find the rotation angle where the overturning moment is largest, and from there test different heel angles around that point. It is important to remember to combine the influence of both wind on topside and 'water'<sup>1</sup> on the hull (see figure 4.1 for system of axes).

As the flow is not entirely uniform across the floor, the hull is raised from the floor surface with dummy cylinders. The extra moment arm contribution must be deducted afterwards.

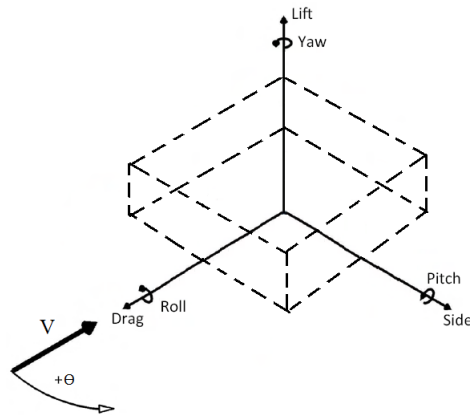


Figure 4.1: System of axes

By experience and results from tests (see figures 4.5 and 4.6), the largest

---

<sup>1</sup>Tests are done in the same wind tunnel as topside with air as the working fluid

overturning moment usually occurs at  $45^\circ$  and with model A it is with the helideck closest to the wind direction, see orientation of model in figure 4.2. Overturning moment is plotted as 'critical angles' in figures 4.5 and 4.6.

In the following chapter, focus will not be on the overturning moment, but on the results obtained experimenting with the tower framework, the platform legs and the boundary layer and what kind of changes that lead to when testing.



Figure 4.2: Model of platform A

## 4.1 Tower framework

As presented in earlier chapters, the geometric shape of an object is of great significance to the aerodynamic properties at various Reynolds numbers. Lattice towers are difficult because a simple downscaling does not necessarily give the desired geometric similarity, and at large model scale ratios, it is not always possible to precisely model the individual members. The local flow through the lattice structure may influence global results if the members are Reynolds number sensitive.

At NTNU, they have a model platform, 'model A' (scale 1:120, figure 4.2). It has a relatively tall triangular tower with a lattice framework, where the design choices for the framework is debated. We want to measure the influence of the geometric design of the members on the measurement data of forces and moments, seeing as the tower has a significant moment arm.

Therefore, two different towers were made to be used for comparison, see figures 4.3 and 4.4 and table 4.1 for details. As we know, from section 2.3.4, similarity to full-scale is easier to achieve with square members, since sharp edges create separation independent of Reynolds number.

With circular geometries, there is a scale effect problem. The local flow past

a circular geometry, such as the lattice tower, in the wind tunnel is generally subcritical versus the flow at full-scale which is post-critical, meaning it has lower  $C_D$  values.

To account for this, different methods such as changing the surface roughness or reducing the diameter are used. Reducing the diameter is only an option when it does not cause a pronounced effect on the wake field, as is the case with larger cylindrical structures e.g. platform legs. Considering tower 2, the diameter of the circular members are smaller than scale.

The data from model A was gathered during this thesis experiments, and the data from model B (1:150) was gathered by NTNU at an earlier time. Measurements are done at a constant wind tunnel velocity of approximately 16 m/s and with zero heel of the model.

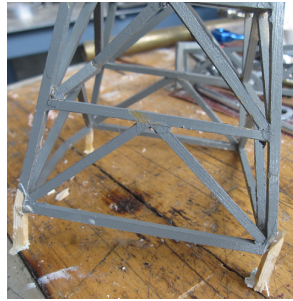


Figure 4.3: Model A, tower 1

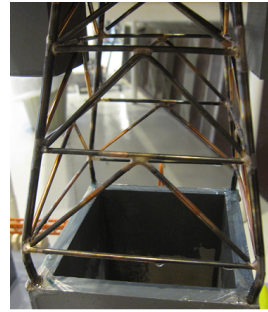


Figure 4.4: Model A, tower 2

	Tower 1	Tower 2
Geometry	Square	Circular
Dimension	In correct scale	Smaller than scale
Material	Painted wood	Steel

Table 4.1: Details of the different towers

Usually, the wind tunnel is fitted with spires to create an atmospheric boundary layer (see section 2.5.1), but in this case of comparing the two towers it felt adequate to use a uniform velocity field with no modification to the flow upstream. Also, the results was to be used later for boundary layer comparisons, with and without the simulated boundary layer in place.

The measurements are done in the large wind tunnel (see section 3.1), using a six component balance to measure forces and moments, and a built-in pressure differential for velocity. Since the velocity is measured in the contraction, we multiply with a factor to get the velocity at reference height by the model.

The dimensions of the model are determined roughly to be a quadratic volume with equal lengths of 0.7 m, even though in reality, the frontal area of the



model changes with rotation. Since the balance set-up was rotated 90 degrees clockwise compared to the standard set-up (see figure 3.2), the side force is at its maximum at the starting position at 0 degree angle.

That means, both equations 2.44 and 2.45 still apply, but the side force correction is used for the drag force and vice versa. The following figures show the results from the experiments, where y-axis = coefficients and x-axis = degrees of rotation from starting position. No blockage corrections are applied to the results.

As we can see from figure 4.7 and 4.8, the difference in values of measured coefficients between tower 1 and tower 2 of model A is visible. The initial prediction was that since the tower itself has such a long moment arm, the difference in moments would be even easier to see than the difference in forces.

We can see from the graph that the influence is greatest for the side and drag force and pitch and roll moment, followed by lift, but the yaw moment is almost the identical. Not surprising, as the tower is centered in the middle of the platform.

We can see from figures 4.9 and 4.10 that the results from model B displays the same tendencies as the results from model A. The tower with the square geometric members generates more side and drag force including pitch and roll moment. Lift and yaw is not affected as much, if at all.

The main objective was to identify the dissimilarity between the two cases, if any. At the same time, it is difficult to determine which of the two geometries is the more accurate or right one to use because of lacking comparable full-scale results.

A possibility is to measure loads separately on individual parts of the model e.g. the tower which makes it easier to find comparable full scale data. The change in the values magnitude does not have an impact on the overall stability analysis, as the critical angles remains the same, but that could change if the tower is positioned off-centre.

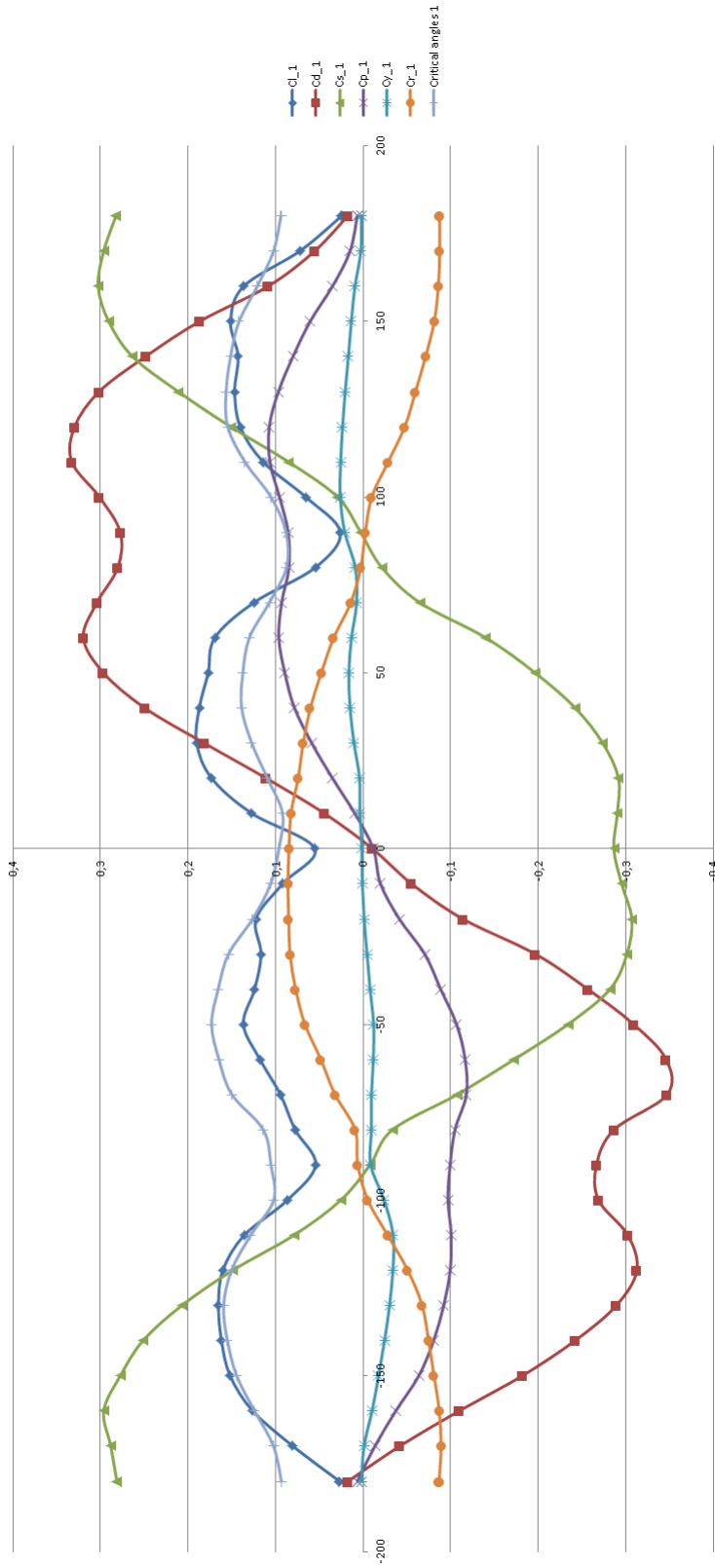


Figure 4.5: Model A, tower 1: forces and moments coefficients

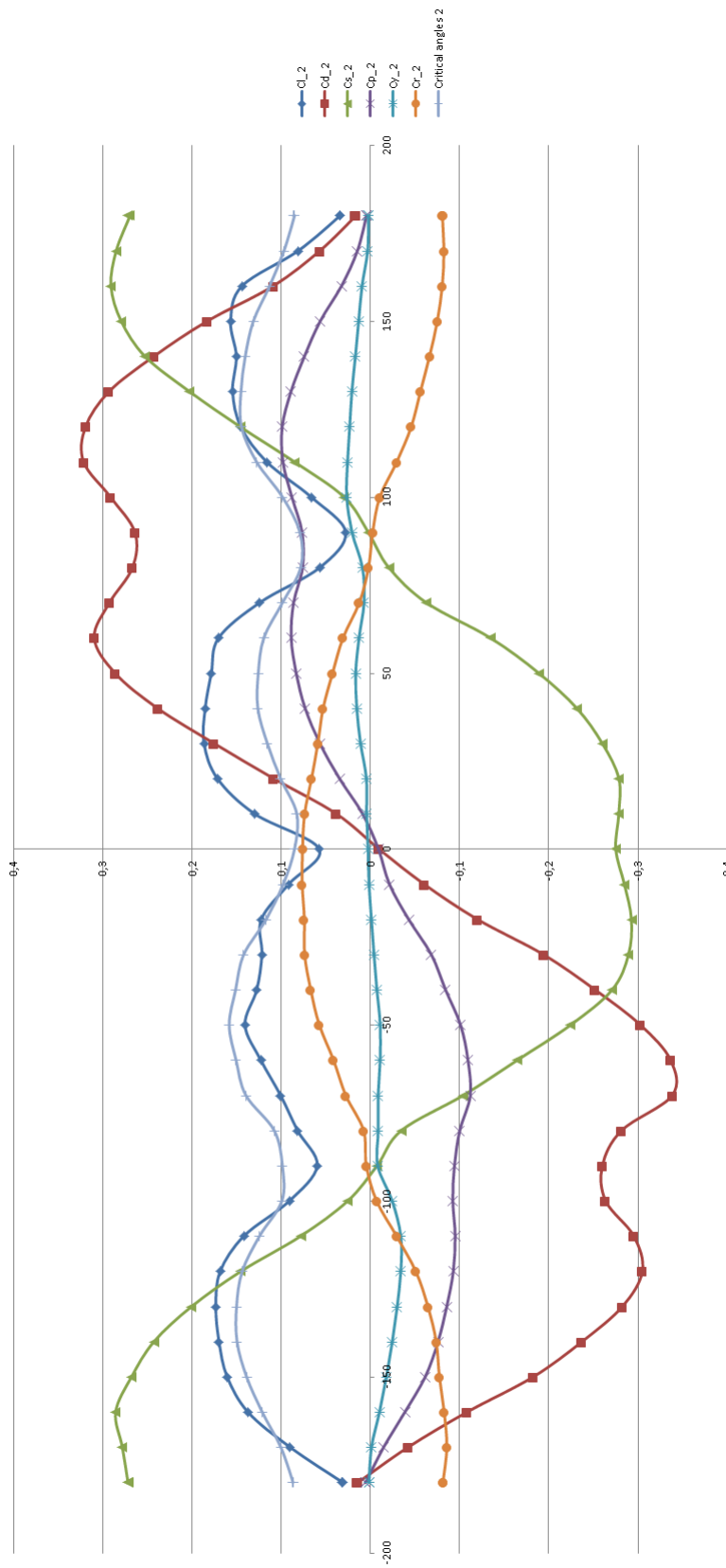


Figure 4.6: Model A, tower 2: forces and moments coefficients

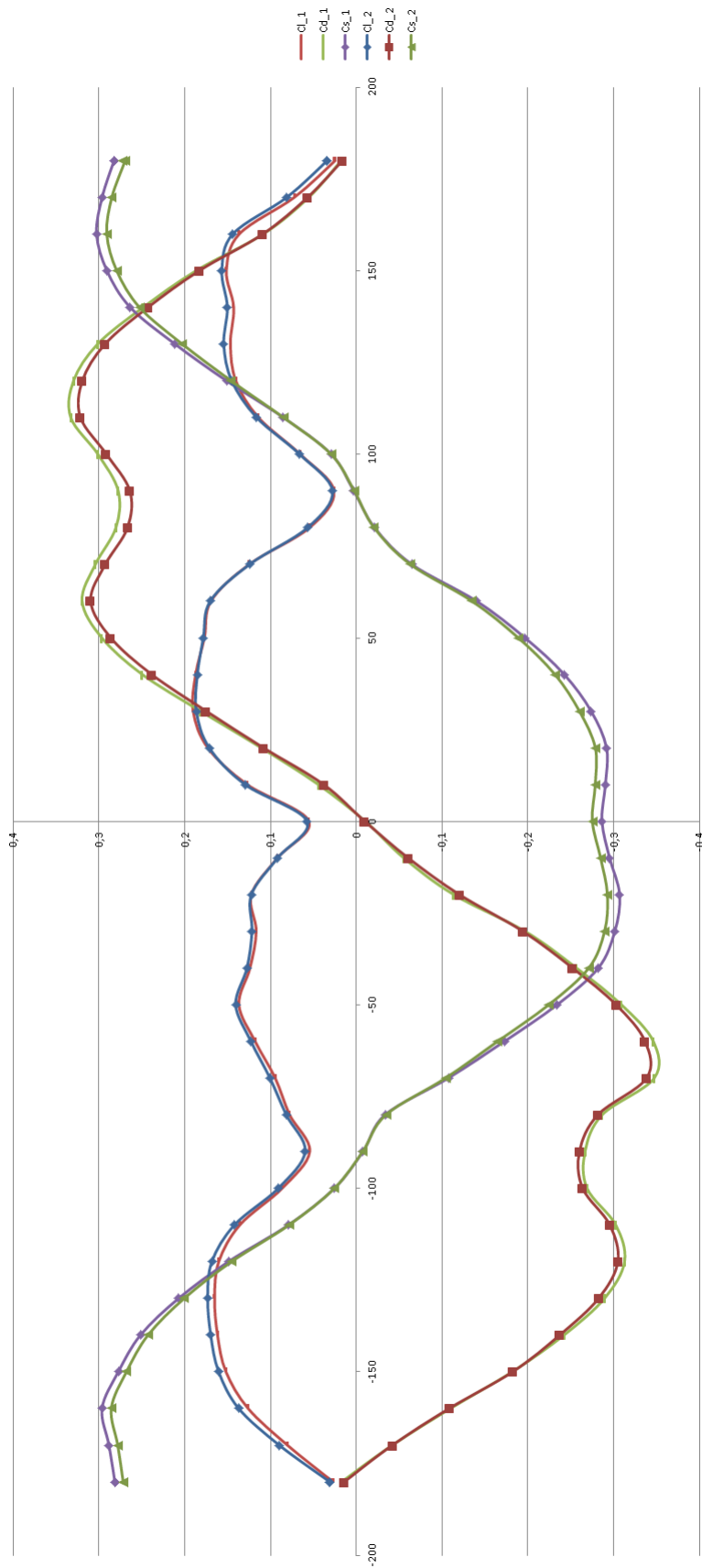


Figure 4.7: Model A, tower 1 and 2 forces comparison

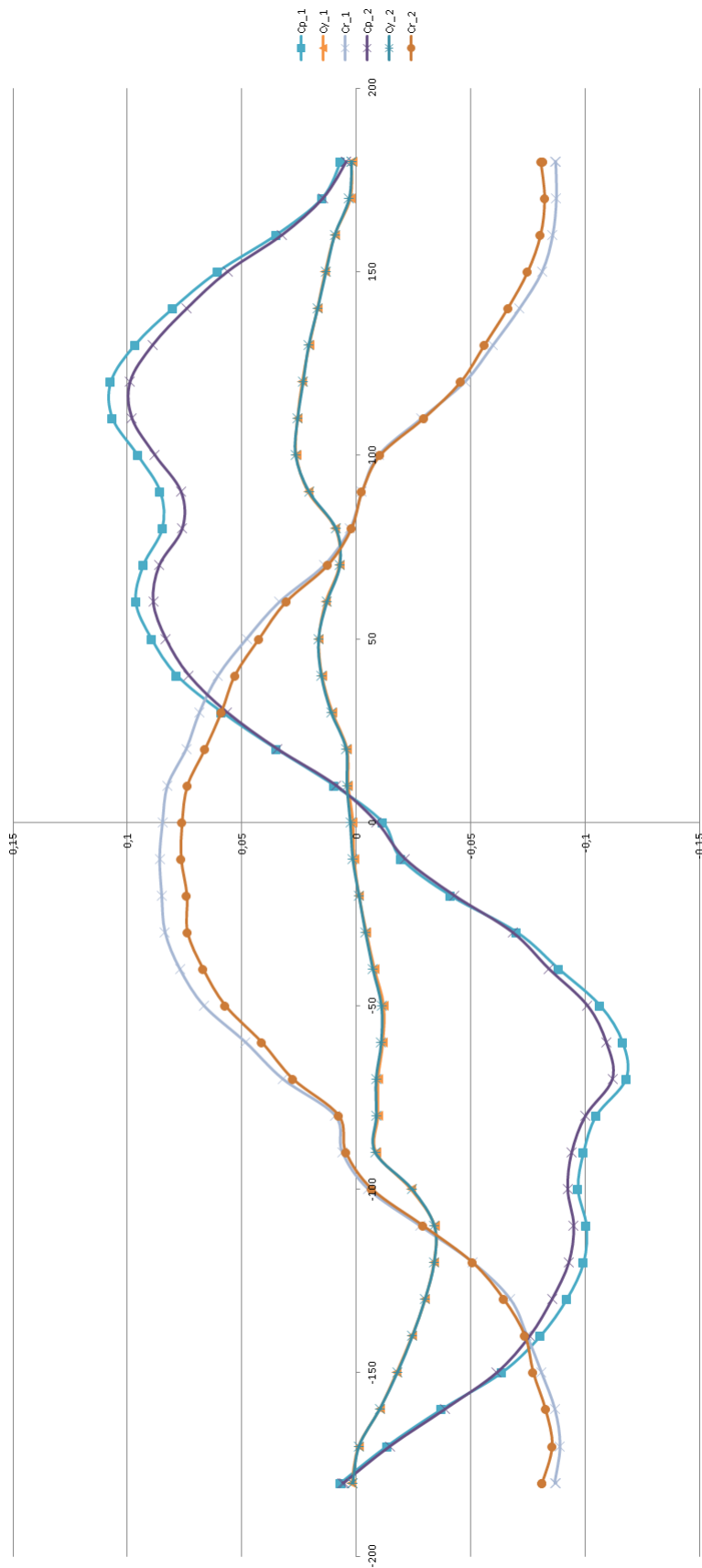


Figure 4.8: Model A, tower 1 and 2 moments comparison

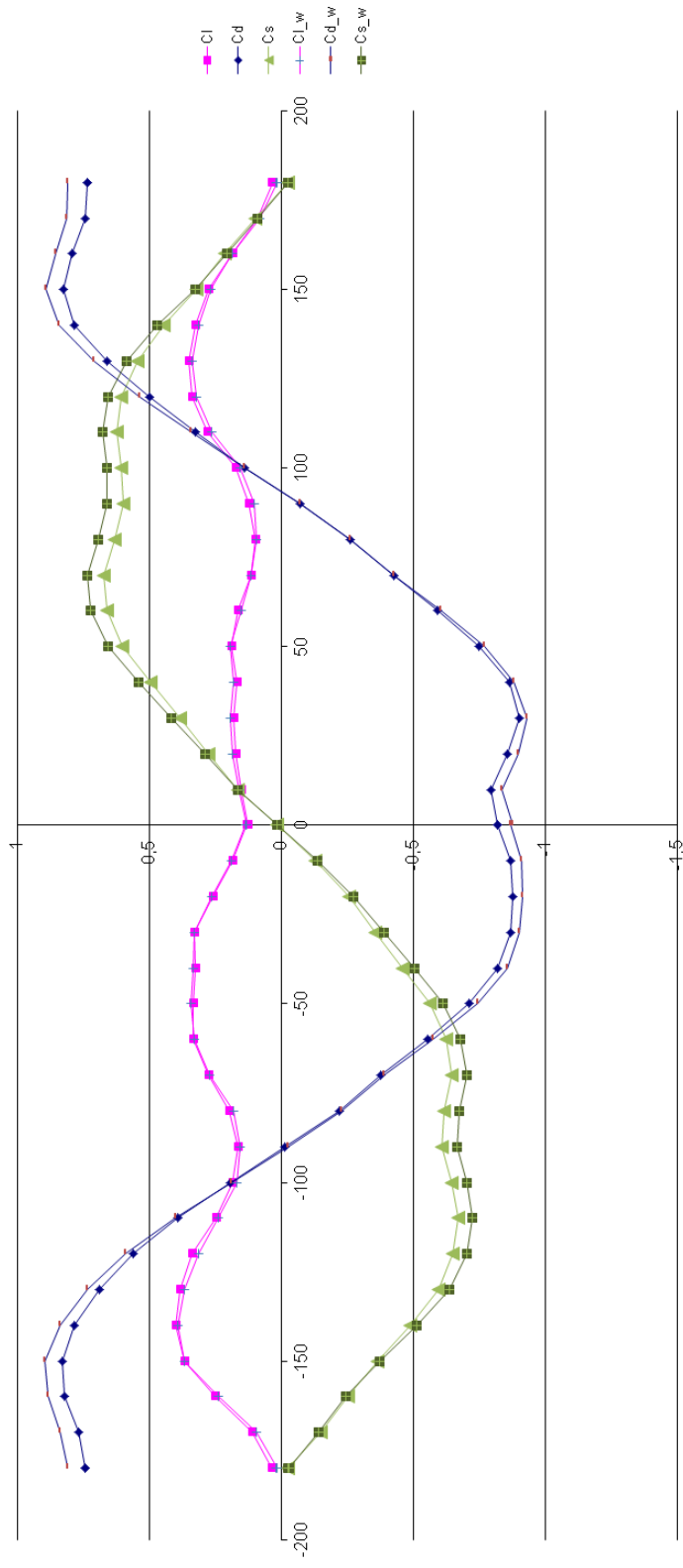


Figure 4.9: Model B, forces comparison between circular and square (subnote w) members

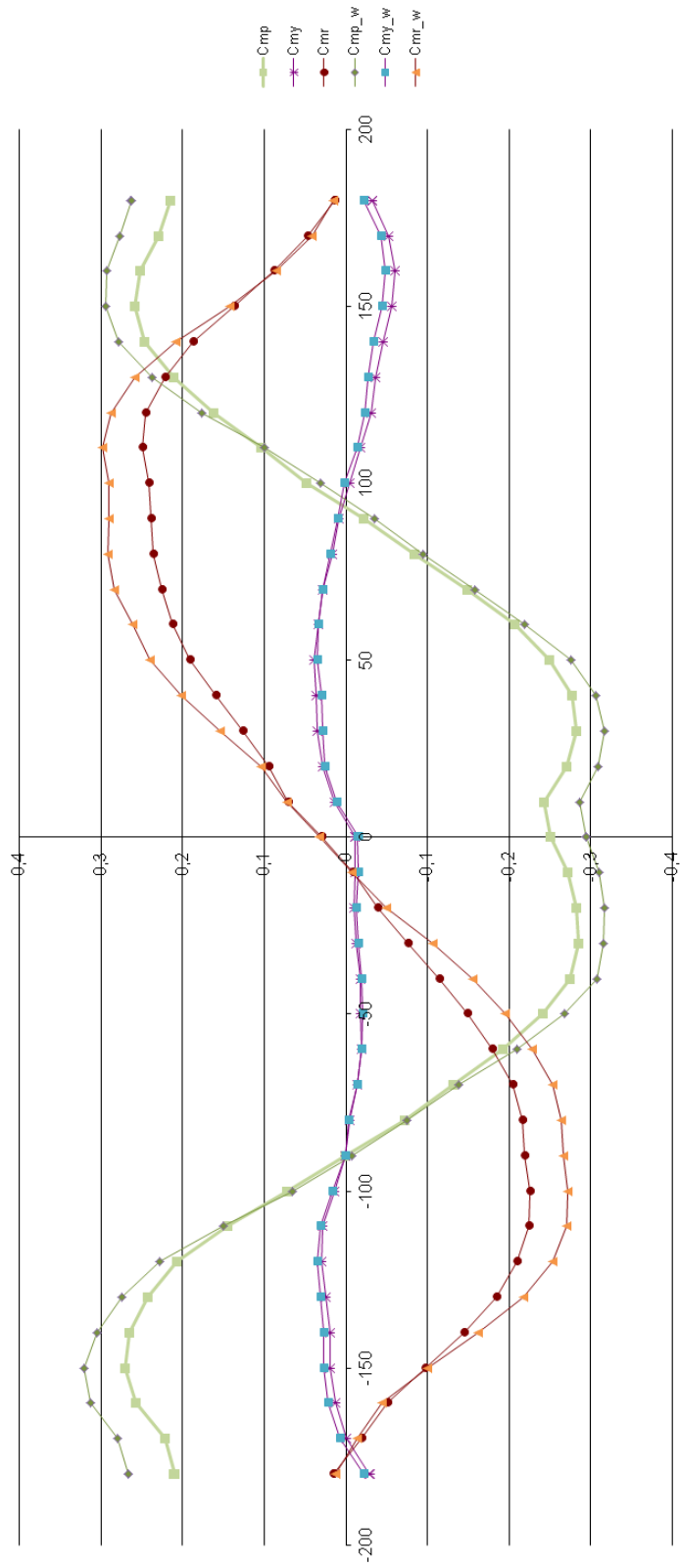


Figure 4.10: Model B, moments comparison between circular and square (subnote w) members

## 4.2 Atmospheric boundary layer

Model A have been tested with tower 1 with and without a simulated atmospheric boundary layer. In reality, friction near the wind tunnel floor will prevent an ideal uniform flow field, but it is regarded as such in the experiments as this effect is considered minimal.

As we can see from figure 4.11 and 4.12, all forces and moments are influenced by the changed flow conditions. The side and drag force, roll and pitch moment have the greatest increase in value in the simulated boundary layer flow versus uniform flow, lift is almost of the same magnitude.

However, the greatest irregularity lies in the measurements of yaw. It is uncertain why. It would be preferable to test model A again with the simulated boundary layer within a shorter time period of testing with uniform flow to see if it has an affect on the results. There is also a noticeable fluctuation in the measurements taken with the simulated boundary layer.

The greatest difference between uniform flow and the atmospheric boundary layer flow is the surface pressure distribution, the magnitude of the velocity and the turbulence intensity in the longitudinal subrange. Also, the correct simulation of suction in separation bubbles are obtained by reproducing high-frequency turbulence.

With a simulated atmospheric boundary layer, the related increased turbulence at the floor surface promotes increased shear stress which gives an increase in skin friction drag, which we can observe from increased values. Because of larger vertical velocity gradients, flow reattachment occurs more frequently and vortex shedding is more organised as a result. Because of the same turbulence which behaves irregularly, varying pressures around the model tend to give fluctuating values.

The pitching moment is larger with the simulated boundary layer, possibly as a result of the height of the resultant force of the flow caused by the velocity profile. The height of the resultant force is lower in the uniform flow, which means the pitching moment will be smaller as a consequence. This applies to the rolling moment as well.

Seeing as the overturning moment is increased with a simulated boundary layer and that it provides a more realistic test condition, it is preferable to keep using a simulated boundary layer in future stability assessments.



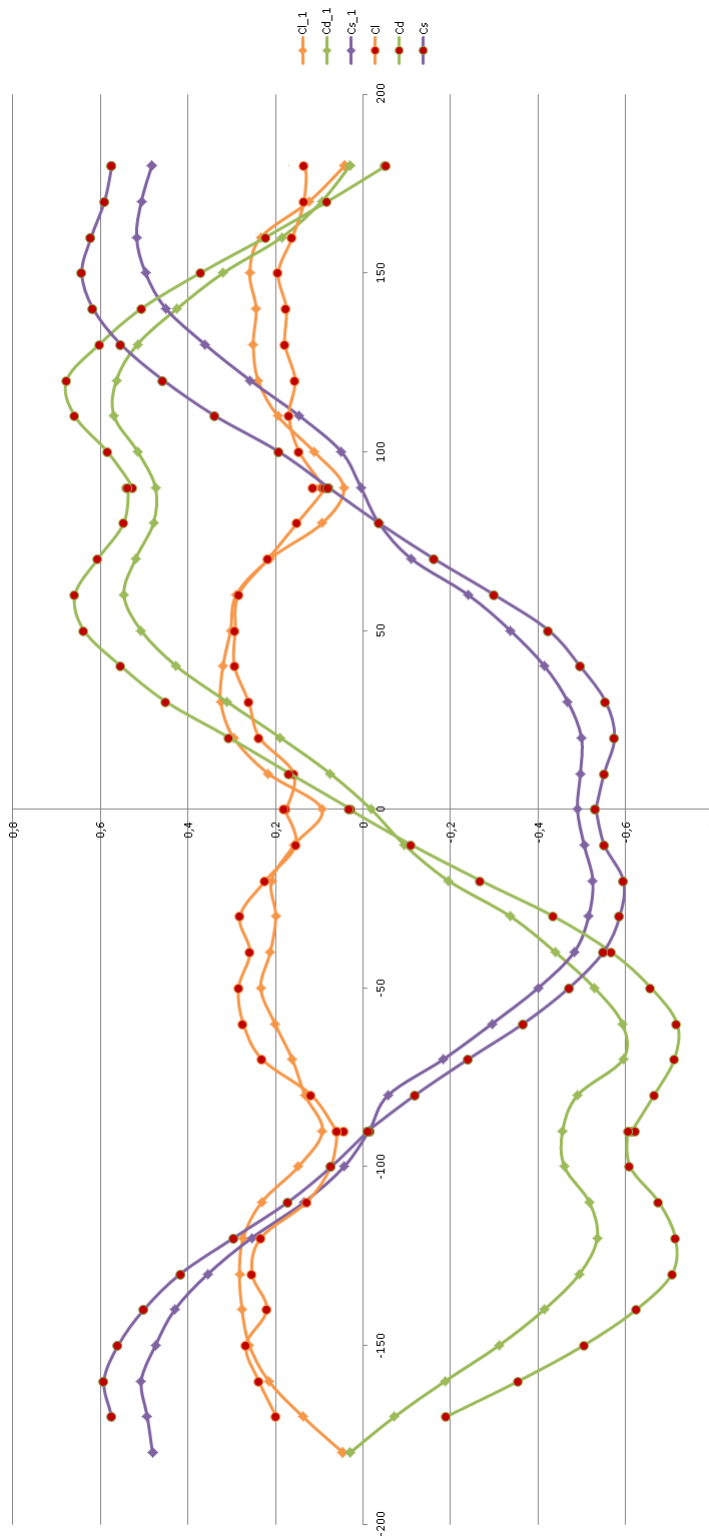


Figure 4.11: Comparison of forces with and without (noted \_1) a simulated atmospheric boundary layer

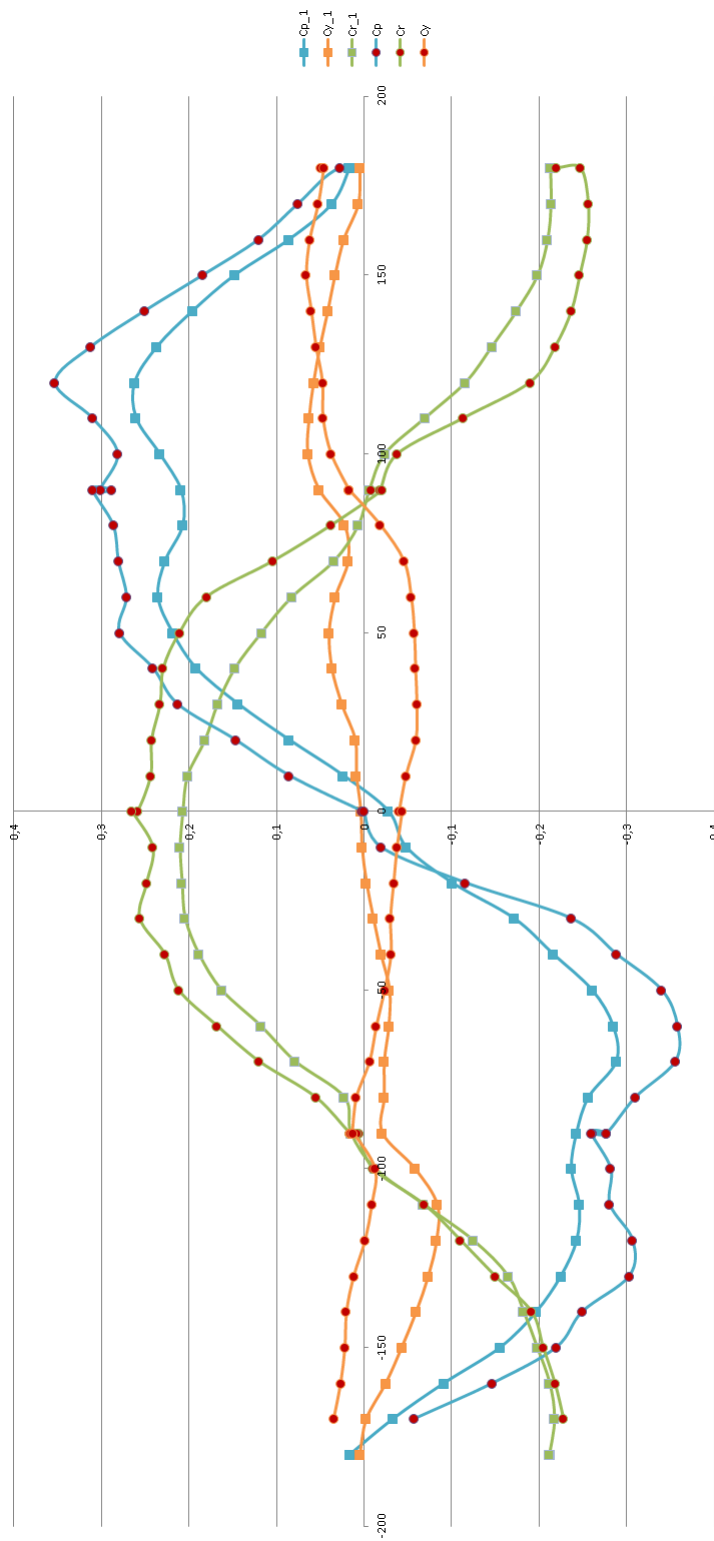


Figure 4.12: Comparison of moments with and without (noted \_1) a simulated atmospheric boundary layer

## 4.3 Flow around a circular cylinder

The flow around cylinders is well-known in fluid mechanics and it is highly dependent on Reynolds number, which affects boundary layer formation, wake width, vortex shedding and the drag force.

In this section, we will look into the design of the platform legs concerning surface roughness and the correlated effect on drag. The wind tunnel used in the experiments is the small wind tunnel, see section 3.1. Dimensions of the cylinder with a circular cross-section is presented in figure 4.13.

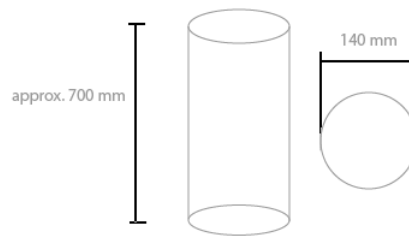


Figure 4.13: Cylinder measurements and cross-section

### 4.3.1 Experiment set-up

The model cylinder was glued to a rod that went through the bottom of the test section floor and was screwed to the three-component balance as shown in figure 4.15.

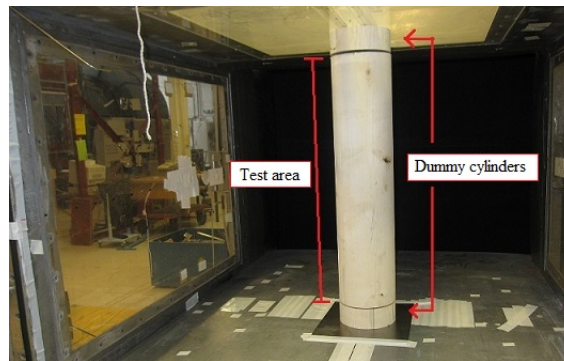


Figure 4.14: Dummy cylinders and boundary layer

It was assumed that the boundary layer generated by the wind tunnel walls was less than 4 cm, so dummy cylinders were mounted to both top and bottom of the cylinder. This is to prevent disturbance from the boundary layer in the

readings (see figure 4.14), and to make sure that the velocity field around my model is uniform.

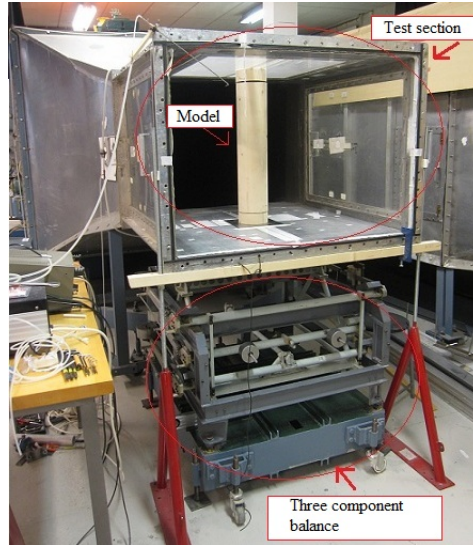


Figure 4.15: Experimental set-up with cylinder

### 4.3.2 Comparison between built-in pressure differential and pitot tube measurements

To check if the measurements from the pressure differential in the built-in pressure differential matched that of the pitot tube measurements (in the small wind tunnel), an experiment was conducted to compare the two. The velocity calculated from the built-in pressure differential is calculated using equation 2.60, and the velocity measured from the pitot tube as a function of the dynamic pressure is calculated with equation 2.62 using the principle of Bernoulli (2.55).

The measurements of the pitot tube had a tendency to give a higher pressure reading than the venturi meter, which led to an average difference in measured velocity to be  $\approx 0.3$  m/s. That could be as a result of poor alignment or placement of the pitot tube or the state of the tubes used. I decided to go with the measurements of the in-built pressure differential in the experiments, as its placement is fixed and does not require probe alignment, thus reducing the error of measurements between tests.

### 4.3.3 Cylinder surface roughness

The effect of surface roughness on the flow is investigated over a Reynolds number range of  $1.6 \cdot 10^4 < Re < 1.8 \cdot 10^5$ . The drag coefficient has been determined as a function of the Reynolds number for two different surfaces. With increasing roughness, the critical Reynolds number decreases, as seen in

figure 4.17. An increase in drag and the critical Reynolds number caused by tunnel blockage has not been accounted for.

We want to reproduce a flow similar to full-scale flow around the cylinder by artificially disturbing the laminar boundary layer that would form on the model surface near the region of separation and change the transition to turbulent flow.



Figure 4.16: Test cylinder surfaces

The two different surfaces will be:

- Standard, plain wood, untreated
  - Nothing additional added to the surface, just the standard material wood with a 'smooth' surface from using a lathe tool
  - Detailed assessment of the roughness of the wood has not been done
- Increased surface roughness
  - A layer of paint is added to the whole surface containing coarse sand elements to make the surface uneven with  $k = 1,25$  mm
  - Sand elements should satisfy equations 2.26 and 2.27, as shown in equations 4.1 and 4.2. They are both valid given velocities above 5 m/s, which is far below the usual velocity range for platform testing

$$\frac{k}{h} = \frac{1.25 \cdot 10^{-3}}{0.14} = 0.893 \cdot 10^{-2} \leq 10^{-2} \quad (4.1)$$

$$\frac{Vk}{\nu} \approx \left( \frac{1 \cdot 1.25 \cdot 10^{-3}}{1.5 \cdot 10^{-5}}, \frac{20 \cdot 1.25 \cdot 10^{-3}}{1.5 \cdot 10^{-5}} \right) = (80, 1600) \geq 400 \quad (4.2)$$

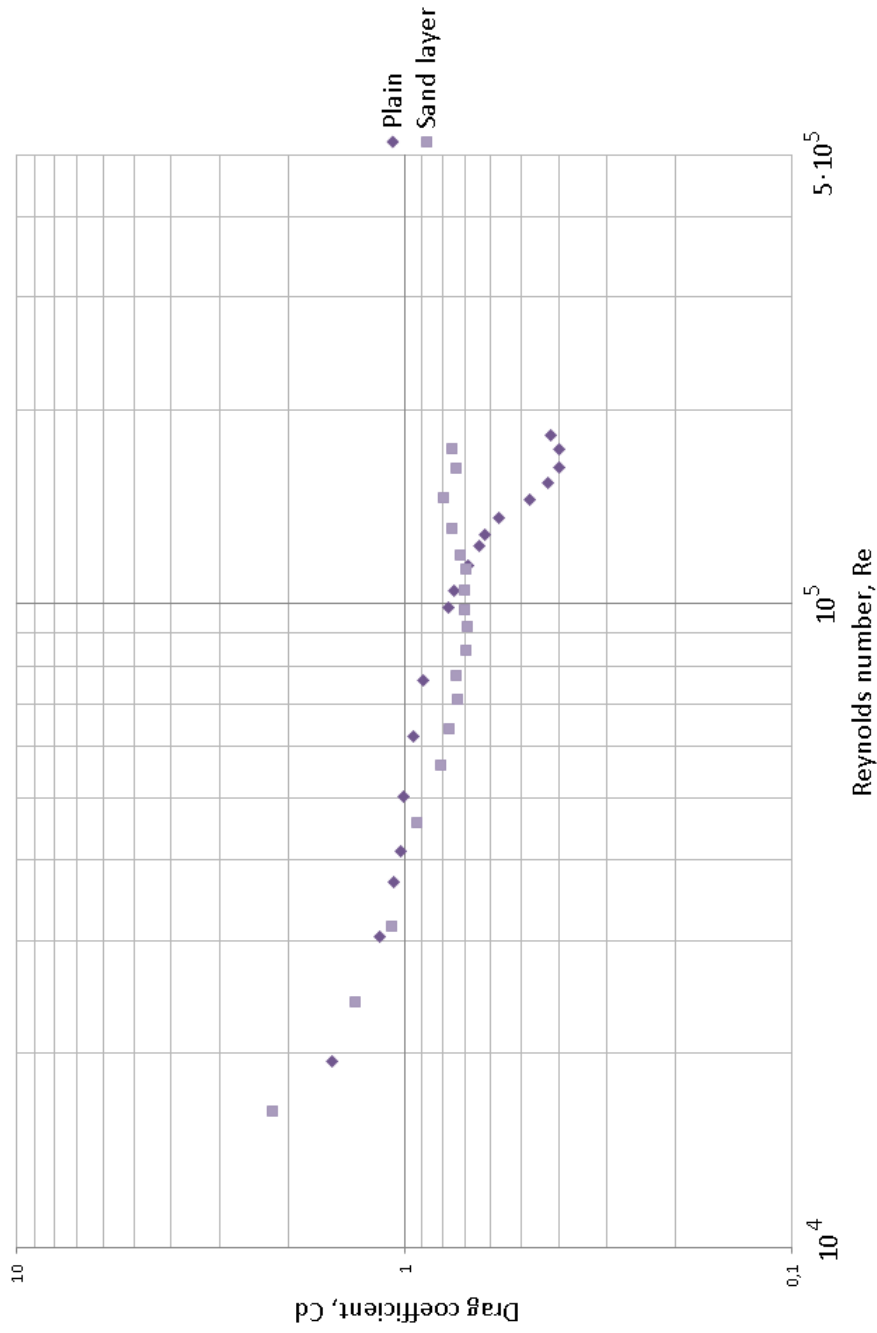


Figure 4.17: Cylinder  $C_D - Re$  data

### 4.3.4 Experimental results and discussion

As we can see from figure 4.17, the profile from the experiment matches that of known theoretical values, as seen in figure 2.5 and we can see that  $C_D \propto Re$ . The transitional area of the plain cylinder is occurring around the Reynolds number of  $1.5 \cdot 10^5$ , while with the increased surface roughness the transition happens earlier. A detailed analysis of the surface roughness of the plain wooden surface was not done, so it is hard to tell what the  $k$  value is, but it is certain it cannot be classified as 'smooth'.

When the sand layer was applied, we can observe an earlier drop in drag at a lower Reynolds number. However, the amplitude of the drop is much less than the plain case. When further increasing the velocity, drag increases again, but is expected to stay below the values in the subcritical range. Based on what we know from similar experiments done by others, with increased velocity, the value for the plain cylinder would be expected to rise as well until it stabilized on a value lower than the subcritical range.

The results from the experiment show that it is possible to calculate the drag coefficient for a circular cylinder reasonably accurate by using a low speed wind tunnel and a simple analog measuring balance. Unfortunately, it was not possible to produce higher velocities, neither was it possible to redo the experiment with a larger cylinder diameter because of possible increased blockage effects, which means experimental data from the supercritical range is limited. However, it covered the approximate Reynolds number range used during platform testing.

More accurate results could have been obtained by measuring the drag force electronically e.g. strain gage-based balance with a more sensitive scale. Also, a more specific air speed indicator could have been preferable.

When experiments with the platform model are conducted in the large wind tunnel, a similar surface as the sandlayer is currently being used on the platform legs. It is reasonable to believe that it contributes to more turbulent flow around the platform legs which is similar to the full-scale flow at a significantly higher Reynolds number. Considering projected values of  $C_D$  at higher Reynolds numbers, it is possible that the value of  $C_D$  for the sandlayered cylinder at the Reynolds number for the test is similar to the full-scale value at higher Reynolds numbers. However, as mentioned earlier, it is difficult to know the exact flow characteristics at full-scale which makes it a qualified guess.

## 4.4 Experimental uncertainty

In order to know how accurate our experimental measurements are, we have to conduct an uncertainty analysis. Uncertainty can come from the measuring device itself, the accuracy of the calibration, signals or the observed value.

We can divide uncertainty into three different types: personal, systematic

and random uncertainties.

Personal uncertainties comes from bias of carelessness in reading an instrument, recording data or in calculations. In error propagation, the only personal error that can be accounted for is the parallax when reading a meter (faulty reading caused by viewing position).

Systematic uncertainty, is a type of bias error, where the results tend to differ in one specific direction. The results will be consistently too high or too low, usually due to imperfections in the equipment. This error can be reduced by improving instrumentation.

Random uncertainties, are unbiased, and can be too high or too low, dependent on the individual measurement. The measured values are spread around a mean value, but will deviate with a certain quantity. To reduce the effect of random uncertainty, one should do a sufficiently number of measurements so that the mean value is as close as possible to the “real” value.

The deviation of measurements due to uncertainty is noted as  $y = (\bar{y}_i \pm W_y)$ , where  $\bar{y}_i$  is the mean measured value and  $W_y$  is the total uncertainty for the subscript variable, calculated from equation 4.3. We are not interested in the individual uncertainties, but the propagation of uncertainties, which means we have to add all uncertainties involved in the value we are interested in.

The error propagation law shown in equation 4.3 is a function of  $f(Y)$ , with the partial derivative of all variables multiplied with the uncertainty of each variable, assuming that each variable is independent of each other. The uncertainty of each individual variable is estimated by reasoning, testing, repeated measurements or manufacturer’s specifications (relative error:  $\frac{W_y}{y}$ , absolute error:  $W_y$ )

$$W_y = \left[ \sum_{j=1}^N \left( \frac{\delta f(Y)}{\delta x_j} \cdot W_j \right)^2 \right]^{1/2} \quad (4.3)$$

Let us take the drag coefficient as an example. As described in the book “Low-speed wind tunnel testing” [13], based on the method of Kline and McClintock [4], the uncertainty of the drag coefficient  $W_{cd}$  is a function of the uncertainty of the measurements, such as pressure, temperature and so on, and of the accuracy of the instruments used. If we use the law of error propagation for the drag coefficient, we get:

$$W_{cd} = \sqrt{\left( \frac{\delta C_d}{\delta F} W_F \right)^2 + \left( \frac{\delta C_d}{\delta \rho} W_\rho \right)^2 + \left( \frac{\delta C_d}{\delta V} W_V \right)^2 + \left( \frac{\delta C_d}{\delta A} W_A \right)^2 + \left( \frac{\delta C_d}{\delta \epsilon} W_\epsilon \right)^2} \quad (4.4)$$

We can simplify the equation by dividing by  $C_d$  and writing out the partial derivatives:



$$\frac{W_{cd}}{C_d} = \sqrt{\left(\frac{W_F}{F}\right)^2 + \left(\frac{W_\rho}{\rho}\right)^2 + \left(\frac{2 \cdot W_V}{V}\right)^2 + \left(\frac{W_A}{A}\right)^2 + \left(\frac{W_\epsilon}{\epsilon}\right)^2} \quad (4.5)$$

Each of the terms is built up of smaller components of uncertainties used to calculate them, see table 4.2. The components may vary depending on the method used to measure them.

Variable	Function of
<b>F</b>	B (voltage output), E (calibration factor), M (weight), g (gravitational constant)
$\rho_{air}$	h (pressure height of Hg barometer), $T_r$ (room temperature)
<b>V</b>	$\Delta p$ (differential pressure), $\rho_{air}$ (air density), $A_r$ (tunnel area ratio)
$\Delta p$	$\rho_{ethanol}$ (ethanol density), g (gravitational constant), x (height of manometer column)
<b>A</b>	b (width), h (height)
$\epsilon$	Assumed theoretical uncertainty

Table 4.2: Components of measurements

When combining all the uncertainties, it is possible to neglect the terms that are relatively small. Most likely, the uncertainty of drag can be simplified to being a combination of uncertainty from force measurements, velocity and the blockage correction factor:

$$\frac{W_{cd}}{C_d} = \sqrt{\left(\frac{W_F}{F}\right)^2 + \left(\frac{2 \cdot W_V}{V}\right)^2 + \left(\frac{W_\epsilon}{\epsilon}\right)^2} \quad (4.6)$$

Due to insufficient knowledge about the quantity of uncertainty related to measurement of force, velocity and blockage, a numerical value is not provided.

# Chapter 5

## Conclusion

Wind tunnel simulations are connected with many problems which result in inaccuracy of the measured aerodynamic values. Even the 'best' wind tunnels are incapable of reproducing the same conditions for the simulation of the flow around the model as the flow in free air. Therefore, finding a way to reduce or eliminate the more prominent problems related to wind tunnel testing is a lasting task, that depends on experimental and theoretical research. Some of the elements have been researched related to testing of model platforms at NTNU in this thesis.

The first problem is the Reynolds number similarity requirement associated with model scaling (1:N). In order for the results to be valid, the Reynolds number need to be the same for the simulated and full scale conditions. An apparent problem is when velocity is the same and the working fluid is air at atmospheric pressure, which means that the Reynolds number will be N times smaller for the wind tunnel simulation, thus altering the flow field conditions e.g. drag.

It is of little concern for sharp-edged features that are Reynolds-number-independent, but plays an important role for features that are Reynolds-number-sensitive. To account for this problem, several modifications to the model have been made to ensure the same characteristics of the flow field even at relatively low Reynolds numbers, which include changing the surface roughness or reducing the scale of certain components.

### 5.1 Platform legs and cylinder drag

The platform legs are cylinders with either circular or rounded square cross-sections. To provoke transitioning from laminar to turbulent flow in the boundary layer surrounding the cylinder and delaying the separation point, reducing the wake and total drag, the surface have been roughened by applying a layer of coarse sand elements.

As seen from the experiments comparing drag before and after applying the

sand layer, the drop in  $C_D$  for the latter happens sooner, but the amplitude of the drop is smaller.

For the plain cylinder, the drop occurs around a Reynolds number of  $1.5 \cdot 10^5$  and the amplitude is greater. Since we want the value of  $C_D$  of the platform legs to represent full scale conditions, we have to make sure that the value of  $C_D$  is correct within the specific Reynolds number range of the experiment. This is fulfilled by applying the sand layer. As it is hard to tell exactly what the value of  $C_D$  is at full scale conditions at such high Reynolds numbers, it is based on an assumption.

## 5.2 Tower framework

The tower framework, or more precisely the members, have been modified to simulate the correct flow conditions. There are two different design options, which is correctly scaled square members or smaller than scale circular members.

An experimental comparison was made between the two by testing forces of drag, side and lift and moments of pitch, roll and yaw on the model platform with each individual tower. The data showed that square members resulted in higher drag and side forces, including pitch and roll moment, while lift and yaw remained practically the same. The last observation is probably because the tower is centered in the middle of the model.

The results from the experiments prove that the geometric design of the tower is of significance to the overall stability analysis. The same results was apparent for both model A and model B. Seeing as the tower make up for a relatively long moment arm, it is not unexpected. The design choice of the tower members will be more important if the tower is positioned off-centre, as it then possible the critical angle will change.

That means that further research should be done on the subject, so that the flow conditions through the lattice tower is accurate. One way to go is to test the tower sections individually.

## 5.3 Atmospheric boundary layer

To be able to get the most accurate results, the wind conditions in the wind tunnel should mimic the conditions of free flow at the test section. This is especially difficult with short wind tunnels where the boundary layer does not have time to develop naturally.

That means we have to simulate the generation of an atmospheric boundary layer in the wind tunnel by artificially disturbing the flow with the use of different types of roughness elements. A comprehensive review has been done by Counihan [6] regarding the atmospheric boundary layer.

At NTNU, the set-up has been decided by trial-and-error. When testing the stability of oil platforms, turbulence spires in combination with a lateral barrier are used to provoke the formation of a thick, uniform and steady boundary layer.

The validity of this is confirmed by comparing results from the velocity profile, turbulence intensity and energy spectrum with theoretical data and guidelines. The method used at NTNU proved a good fit.

## 5.4 Wind tunnel blockage

There are many parameters to consider when calculating blockage corrections. The primary consideration is solid and wake blockage caused by wall interference. Opposed to free flow, flow in the tunnel is constricted by the surrounding walls when encountering an object.

The blockage effect depends on the ratio between model area  $S$  and tunnel area  $A$ , as seen in figure 2.16. According to Pope [13], the blockage ratio should not exceed 10% to avoid faulty measurements.  $\frac{S}{A} \approx 0.10$  for the model platforms and the cylinder, calculated with an overestimation of the model area, which makes it acceptable as it is just below the recommended value.

Several methods have been presented to correct coefficients with regard to blockage, where Pope is the simplest and uses a general approach to bluff body correction. The method of Maskell originates from data taken from experiments with a flat plate and the other are deviations from that. NTNU has used a method similar to that of Maskell with the values taken from appendix B.

It is apparent, that still today, blockage corrections are not fully understood and there does not exist one universal method, but the consensus of opinion seems to be that Pope's criteria of area ratio should be fulfilled.

The obvious benefit to be able to accurately correct for wind tunnel blockage is that it opens the possibility to increase the size of test models or minimize the size of wind tunnels, thus reducing the space needed for testing.

## 5.5 Uncertainty

As with all experiments, there exist an uncertainty with all measurements that states how accurate the end results are. There are many uncertainties associated with the experiment and to account for them all is beyond the scope of this thesis. An uncertainty assessment should be made so that it can be stated with the results from testing.

## 5.6 Concluding remarks

Overall, the accuracy of predictions from experiments with the model platform depends on how well the flow around the model reproduces full scale i.e. fulfills the requirements of similarity. Geometric similarity is the basis of experimentation and is the area that needs to be improved. The current sand layer on the platform legs have proved to increase turbulent flow and is expected to fulfill the requirements.

On the other hand, testing of the platform tower should be done separately with the intent to identify what kind of cross-sectional area of the members that give the most realistic results, seeing as they make up for a large part of the moment arm. Usually, it is harder to get Reynolds number similarity with circular cross-sections at that scale. It is worth mentioning that even though the results differed in value, the critical angles remained the same. Regarding wall interference, it could be interesting to do a detailed assessment of the boundary layer flow developed at the walls, or do tests with an increasingly larger blockage ratio.

Accuracy can also be validated by comparing test of the same type taken at different times to check the reproducibility. As with the large deviation in yaw produced with and without the boundary layer when doing tests with model A, a similar test should be taken again to reduce the probability of time-of-test-based error.

## Further work

- As the frontal area of the platform model changes with rotation, a re-evaluation should be done with the data with a dynamic area to calculate the coefficients. Based on simple trigonometry, at a  $45^\circ$  rotation from the starting position, the frontal area of the model increases with approximately 70%
- In this thesis, when calculating blockage corrections, only side and drag forces were considered. One way is to use the simple correction of Pope applied to the overall velocity, or find out how wall interference affect the forces and moments individually, but it is difficult to know to what degree they are affected
- Another test comparing the flow with and without a simulated atmospheric boundary layer should be made within a shorter time-period to see if the same results and irregularities occur
- Do a detailed uncertainty analysis based on the law of error propagation

# Bibliography

- [1] Esdu 80024: Blockage corrections for bluff bodies in confined flows.
- [2] Elmar Achenbach. The effects of surface roughness and tunnel blockage on flow past spheres. 1973.
- [3] D. Althaus. Tunnel-wall corrections at the laminar wind tunnel.
- [4] Kline B.F. and McClintock F. A. Describing uncertainties in single-sample experiments. *Mechanical Engineering*, page 3, 1953.
- [5] Kevin Cooper. Bluff-body blockage corrections in closed- and open-test-section wind tunnels. *Wind tunnel wall corrections, AGARD-336*, 1998.
- [6] J. Counihan. Adiabatic atmospheric boundary layers: a review and analysis of data from the period 1880-1972. 1975.
- [7] Norwegian Maritime Directorates. Norwegian maritime directorates regulations for mobile offshore units, part vi g, regulations of 4 september 1987 no. 856 concerning construction of mobile offshore units, appendix ii. *NMD*, 1987.
- [8] S. Emeis. How well does a power law fit to a diabatic boundary-layer wind profile? 2005.
- [9] J. C. R. Hunt and H. Fernholz. Wind-tunnel simulation of the atmospheric boundary layer: a report on euromech 50 (part 3, p543-559). 1974.
- [10] Aaron Altman Ian Ross. Wind tunnel blockage corrections: review and application to savonius vertical-axis wind turbines. 2011.
- [11] H. P. Irwin. The design of spires for wind simulation. *Journal of Wind Engineering and Industrial Aerodynamics*, pages 361–366, 1981.
- [12] G. Barnaud J. Gandemer and J. Biétry. *Étude de la tour D.M.A., Partie 1, Étude des efforts dus au vent sur les façades*. Centre Scientifique et Technique du Bâtiment, Nantes, France, 1975.
- [13] Jr. Jewel B. Barlow, William H. Rae and Alan Pope. *Low-speed wind tunnel testing*. John Wiley & Sons, 1999.

- [14] M.F.P. Lopes, M. Glória Gomes, and João G. Ferreira. Simulation of the atmospheric boundary layer for model testing in a short wind tunnel. *Experimental Techniques*, 32:36–43, 2008.
- [15] Princeton. [http : //www.princeton.edu/ asmits/bicycleweb/blunt.html](http://www.princeton.edu/~asmits/bicycleweb/blunt.html).
- [16] Emil Simiu & Robert H. Scanlan. *Wind Effects on Structures: An Introduction to Wind Engineering*. John Wiley & Sons, 1978.
- [17] Emil Simiu. Toward a standard on the wind tunnel method. *National Institute of Standards and Technology Gaithersburg, MD 20899-8611*, 2009.
- [18] Wei and Desmond. Atmospheric boundary layer wind tunnel design. *Turbulence Energy & Combustion Group, University of Adelaide, Australia*.
- [19] Frank M. White. *Fluid Mechanics*. McGraw-Hill, 6th edition, 2008.
- [20] Bradley Wooding and Marshal. Drag due to regular arrays of roughness elements of varying geometry. *Boundary layer meteorology*, page 285, 1973.



## Appendix A

# NMD Regulations

**NORWEGIAN MARITIME DIRECTORATES REGULATIONS FOR MOBILE OFFSHORE UNITS, PART VI G, REGULATIONS OF 4 SEPTEMBER 1987 NO. 856 CONCERNING CONSTRUCTION OF MOBILE OFFSHORE UNITS, APPENDIX II:**

**Appendix to §8 - Wind tunnel test procedure**

**Laboratory**

The wind tunnel test shall be carried out by a recognized institution.

**Model**

The model should include all structural details and equipment fitted, which may effect the result of the wind tunnel tests. Separate tests should be performed for the above water construction and the underwater body. The anchors should be at the bolsters, and the cranes in the stowed position. Pipes and pipe-handling equipment in the derrick should be considered.

**Wind profile**

The above water part of the model should be exposed to a simulated natural ocean wind. Reference height for velocities should be 10 m above water level. The mean velocity profile should be according to the power law:

$$\frac{V_H}{V_{10}} = \left[ \frac{H}{10} \right]^\alpha$$

$V_H$  Mean velocity at height H above water level, (m)

$V_{10}$  Velocity at reference height. (10 m)

H Height above water level. (m)

$\alpha$  Exponent chosen to represent ocean wind. Should be within the range 0.11 - 0.14

Curves showing both the measured velocity profile and the velocity profile corresponding to the power law should be shown in the report.

The turbulence intensity profile in the wind direction of the simulated wind should also be considered. The turbulence intensity should accordingly be measured in the wind tunnel and plotted as a function of the height above the sea level.

The underwater body should be exposed to uniform wind (alternatively, model tests in a water basin may be performed).

**Scale effects**

Provision should be made to ensure the same character of the flow in the model scale as in the full-scale conditions. This should be documented by measurements at various Reynolds numbers for the above water construction and the underwater body. Curves should be included in the report.

**Measurements**

Three forces and three moments (corresponding to the main axis) should be measured for each test run, and the results presented as nondimensional coefficients. The instruments should be calibrated prior to each trial. The calibration before and after a test series should give the same results. If not, retesting is necessary.

### Critical axis

The wind direction at which the highest wind overturning moments will be encountered, shall be determined on the basis of a test of each draught applicable (see item 7). The combined results of the above water construction and the underwater body have to be considered.

The wind direction shall be changed in steps of preferably 10 degrees from 0 to 360 degrees. Moment coefficients etc. shall be shown in a diagram.

- 6.1. Overturning moments corresponding to the axis at which the maximum moment occurs (critical axis) should preferably be used for any wind direction in the stability analysis.
- 6.2. If the moments corresponding to 6.1 are judged to be too conservative for the damage stability calculations, additional tests for each damage case not treated according to 6.1 have to be performed. The critical axis should be chosen according to the damage stability calculations without wind.
- 6.3. If the moments according to 6.1 are judged to be too conservative for intact stability, a similar approach as for 6.2 has to be agreed upon, taking the stability characteristics of the unit into consideration.

### Tests

Tests of the underwater body as well as the above water construction have to be carried out for a sufficient number of draughts to establish wind moment curves as a function of the draught. At least maximum drilling draught, survival draught (or a similar draught if survival draught not is applicable) and transit draught have to be considered.

For the critical axis according to 6.2 at least two draughts shall be considered for each damage case.

For each draught, tests shall be performed for at least three, but preferably four inclination angles (for example 0, 5, 15 and 20 degrees).

The wind direction shall be perpendicular to the critical axis, but also test runs at directions 10, 20 and 30 degrees to each side of the perpendicular shall be performed and the maximum moment component corresponding to the critical axis should be determined. The reason for testing at wind directions 10, 20 and 30 degrees to each side of the critical wind direction is to be sure to use the maximum overturning moment for the inclined conditions.

Curves showing heeling moments as a function of the inclination angles for each test draught shall be drawn.

In addition curves showing heeling moments as a function of the draught shall be worked out for each inclination angle.

### Adaptations

Depending on the stability characteristics of a particular platform, alterations in the above procedure may be agreed upon. For example, the longitudinal axis for drilling ships should be taken as the critical axis.

### Documentation

The test results including wind forces and moments should be submitted together with sufficient explanatory information and the concluding remarks of the test results. Pictures of the model prior to the tests as well as at each test condition should be included.

## Appendix B

# Maskell's correction factors

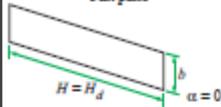

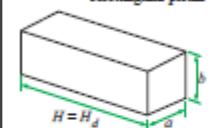
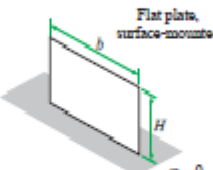
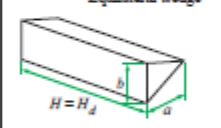
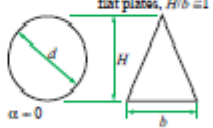
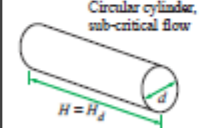
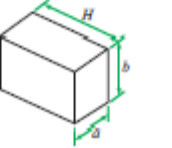

Body shape	$\epsilon$ ; $m$ ; maximum $S/A$	Body shape	$\epsilon$ ; $m$ ; maximum $S/A$
 <p>Flat plate <math>H = H_d</math> <math>\alpha = 0</math></p>	$\epsilon = 0.96$ ; $m = 1.85$ ; for $S/A \leq 0.25$	 <p>Flat plate, centre-mounted <math>\alpha = 0</math></p>	$\epsilon = 2.84 - 0.07H/b$ and $m = 3.20 - 0.05H/b$ for $H/b \leq 20$ ; for $S/A \leq 0.10$ .
 <p>Rectangular prism <math>H = H_d</math></p>	$\epsilon = 1.11 + 0.94a/b$ for $0.2 < a/b < 0.6$ ; $\epsilon = 1.11 - 0.14a/b$ for $0.75 < a/b < 3$ ; for $S/A \leq 0.20$ .	 <p>Flat plate, surface-mounted <math>\alpha = 0</math></p>	$\epsilon \approx 2.37$ ; $m \approx 2.84$ for $\frac{1}{3} \leq H/b \leq 3$ ; for $S/A \leq 0.10$ For $H/b > 3$ use value for centre-mounted plate of $2H/b$ aspect ratio.
 <p>Equilateral wedge <math>H = H_d</math></p>	$\epsilon = 0.98$ ; $m = 2.06$ ; for $S/A \leq 0.20$	 <p>Non-circular, triangular flat plates, <math>H/b = 1</math> <math>\alpha = 0</math></p>	Use value for rectangular plate of same $H/b$ ; for $S/A \leq 0.15$
 <p>Circular cylinder, sub-critical flow <math>H = H_d</math></p>	$m = 1.38$ ; for $S/A \leq 0.20$	 <p>Rectangular block</p>	Use value for flat plate of same $H/b$ provided flow reattachment does not occur, $a/b \leq 2.5$ ; for $S/A \leq 0.10$ .
 <p>Lattice, open area ratio <math>\approx 0.5</math></p>	$m = 1.30$ ; for $S/A \leq 0.10$		

Figure B.1: Blockage correction factors,  $\epsilon$  and  $m$  given a certain aspect ratio  $\frac{S}{A}$   
(left) Two-dimensional flow (right) Three-dimensional flow [1]